






RESEARCH ARTICLE

10.1029/2018JD030076

Laboratory Experiments of Volcanic Ash Resuspension by Wind

V. Etyemezian¹ , J. A. Gillies² , L. G. Mastin³ , A. Crawford⁴ , R. Hasson⁵, A. R. Van Eaton³ , and G. Nikolich¹¹Desert Research Institute, Las Vegas, NV, USA, ²Desert Research Institute, Reno, NV, USA, ³Cascades Volcano Observatory, U.S. Geological Survey, Vancouver, WA, USA, ⁴National Oceanic and Atmospheric Administration, College Park, MD, USA, ⁵Environmental Management Consolidated Business Center, U.S. Department of Energy, Cincinnati, OH, USA

Key Points:

- Laboratory experiments show that volcanic ash deposits are highly wind erodible, with resuspension comparable to the most erodible soils
- Humidity and the addition of liquid water impact ash resuspension in complex ways
- Resuspendable particles are emitted at a rate proportional to the shear velocity raised to a power of 2.9–5.3

Correspondence to:

V. Etyemezian,
vic@dri.edu

Citation:

Etyemezian, V., Gillies, J. A., Mastin, L. G., Crawford, A., Hasson, R., Van Eaton, A. R., & Nikolich, G. (2019). Laboratory experiments of volcanic ash resuspension by wind. *Journal of Geophysical Research: Atmospheres*, 124, 9534–9560. <https://doi.org/10.1029/2018JD030076>

Received 28 NOV 2018

Accepted 1 AUG 2019

Accepted article online 7 AUG 2019

Published online 23 AUG 2019

Abstract Fresh volcanic eruption deposits tend to be loose, bare, and readily resuspended by wind. Major resuspension events in Patagonia, Iceland, and Alaska have lofted ash clouds with potential to impact aircraft, infrastructure, and downwind communities. However, poor constraints on this resuspension process limit our ability to model this phenomenon. Here, we present laboratory experiments measuring threshold shear velocities and emission rates of resuspended ash under different environmental conditions, including relative humidity of 25–75% and simulated rainfall with subsequent drying. Eruption deposits were replicated using ash collected from two major eruptions: the 18 May 1980 eruption of Mount St. Helens and the 1912 eruption of Novarupta, in Alaska's Valley of Ten Thousand Smokes. Samples were conditioned in a laboratory chamber and prepared with bulk deposit densities of 1,300–1,500 kg/m³. A control sample of dune sand was included for comparison. The deposits were subjected to different wind speeds using a modified PI-SWERL[®] instrument. Under a constant relative humidity of 50% and shear velocities 0.4–0.8 m/s, PM₁₀ emission by resuspension ranged from 10 to >100 mg·m⁻²·s⁻¹. Addition of liquid water equivalent to 5 mm of rainfall had little lasting effect on Mount St. Helens wind erosion potential, while the Valley of Ten Thousand Smokes deposits exhibited lower emissions for at least 12 days. The results indicate that particle resuspension due to wind erosion from ash deposits potentially exceeds that of most desert surfaces and approaches some of the highest emissions ever measured.

Plain Language Summary Immediately after a volcanic eruption, freshly deposited ash can be lifted by wind similar to how dust is suspended by wind in arid regions. These “resuspended” ash particles are smaller than the original, more clumpy material that fell during the eruption and are abundant enough to impact human health, visibility, and industrial processes. This is known to happen because it has been observed in the field, but there has been little direct measurement of how much ash can be resuspended at various wind speeds. In the present study, we used a small wind tunnel-like device (PI-SWERL) to measure resuspension of ash. Samples were collected from two locations: the Valley of Ten Thousand Smokes in Alaska (site of the 1912 Novarupta eruption) and deposits from the Mount St. Helens 1980 eruption. The potential for resuspension was measured at multiple simulated wind speed equivalents and under several conditions of atmospheric humidity. Overall, it was found that the Valley of Ten Thousand Smokes samples were more influenced by atmospheric humidity as well as the presence of liquid water a few centimeters below the surface than the Mount St. Helens samples. The latter exhibited the potential for extremely high resuspension rates, approaching the highest that have ever been measured for arid soil surfaces. Vegetation, compaction over time, and other environmental processes likely have a large role in reducing what would otherwise be extraordinary emissions of ash for weeks to years following a volcanic eruption.

1. Introduction

Resuspension of volcanic ash deposits by wind can cause a serious environmental hazard (Liu et al., 2014). High concentrations of lofted ash particles may adversely impact human health (Baxter, 1999; Gordian et al., 1996; Wilson et al., 2011), aircraft operations (Guffanti et al., 2009; Hadley et al., 2004), and infrastructure (Barsotti et al., 2010). Two areas prone to these hazards in North America include the Valley of Ten Thousand Smokes (VTTS) in Alaska and Mount St. Helens (MSH) in the Cascade Range of Washington

State. In Alaska, the Anchorage Volcanic Ash Advisory Center typically issues one or two aviation advisories every year for resuspended ash in the VTTS (Wallace & Schwaiger, 2019). In Washington State, the 18 May 1980 eruption of MSH sent more than 1 km^3 of tephra across Washington, Idaho, and Montana (Sarna-Wojcicki et al., 1981). For weeks after the eruption, multiple wind storms raised airborne ash concentrations above the emergency threshold of $875 \mu\text{g}/\text{m}^3$ and tripled hospital visits (Bernstein et al., 1986; Hobbs et al., 1983). The deposit's dispersal axis also crossed $\sim 100 \text{ km}$ north of the Hanford nuclear site in eastern Washington, leaving $\sim 1 \text{ mm}$ of ashfall on site. A future eruption of MSH represents a potential disruption to operations at the Hanford nuclear site. Specifically, a volcanic eruption may present a hazard from ash depositing from an airborne plume (USGS, 2018) and its resuspension following deposition. Ongoing research efforts by the U.S. Geological Survey and National Oceanic and Atmospheric Administration using predictive models are providing better understanding and characterization of volcanic eruptions, resultant ash clouds, and subsequent ash deposition and resuspension that may impact the region. The work presented here was conducted in support of better estimating resuspension potential following an eruption.

Over the past decade, several major ash resuspension events have been documented globally, including Chile and Argentina (Folch et al., 2014; Reckziegel et al., 2016), Iceland (Arnalds et al., 2013; Beckett et al., 2017; Liu et al., 2014; Thorsteinsson et al., 2012) and Alaska (Schwaiger & Wallace, 2015). However, numerical models of ash transport use poorly constrained assumptions about the deposit emission rates under different environmental and atmospheric conditions (refer to section 2.2 for more detail). Previous laboratory experiments have focused on soil and dust (e.g., Fécan et al., 1999; Marticorena & Bergametti, 1995), but eruption deposits present a unique set of material properties. New experimental work is required to constrain the resuspension behavior of volcanic ash.

In this paper, we quantify the resuspension potential of volcanic ash from MSH and VTTS with experiments in a humidity-controlled chamber. Section 2 provides a review of the relevant literature and theory underpinning resuspension research. Then in section 3, we introduce our laboratory experiments. The overall aim is to provide improved constraints on the key variables used in numerical models, which may be applied to short-term forecasting and long-term hazard assessments in volcanically active regions.

2. Background

Close to a volcano, post-eruptive erosion and remobilization by wind of ashfall and pyroclastic deposits are maximized by large erupted volumes, abundant unconsolidated ash material, destruction of the vegetation cover, and the inhibition of vegetation regrowth (Manville & Wilson, 2004). Farther from the source volcano, at distances of hundreds of kilometers, the potential for resuspension of the deposited ash by wind will be controlled by the depth of the deposit, the particle size distribution of the ash, the moisture conditions during and subsequent to deposition, and the nature of the surface onto which it deposits. An increasing presence of large roughness elements, including vegetation or man-made structures, will increasingly shelter ash from the erosive power of the wind. However, the ash that deposits onto the roughness itself may be very susceptible to resuspension by wind.

2.1. Particle Entrainment Threshold and Emission Flux

Ash particles can be mineral or glass, are in the same size range as mineral particles derived from earth sediments, and exist in some state of consolidation (loosely to tightly bound together) upon deposition. Given these similarities between ash particles and mineral particles derived from earth sediments, the scientific framework that forms our current understanding of wind erosion and dust emissions is a logical lens through which to examine the physics of entrainment of deposited ash particles by wind.

2.1.1. Force Balance on a Particle

Winds capable of entraining particles from the surface are invariably turbulent. To explain the entrainment of particles by shear stress in turbulent flow, a force balance model has typically been invoked for particles (e.g., Bagnold, 1941; Iversen & White, 1982; Lu et al., 2005; Shao, 2000). The theory is expressed simply as

$$u_{*t} = A\sqrt{d}, \quad (1)$$

where u_{*t} is (minimum) threshold shear velocity for particle movement, d is particle diameter, and A is a constant that depends on the density of the particles, density of the fluid, the units used for d , and the

gravitational constant. Based on the theory of the “law of the wall” (Prandtl, 1935), in a well-developed boundary layer, shear velocity (u_*) is proportional to the square root of the ratio of wall shear stress to fluid density

$$u_* = \sqrt{\frac{\tau}{\rho_{\text{air}}}}, \quad (2)$$

where τ (N/m^2) is the wall shear stress and ρ_{air} is the density of air (kg/m^3).

This model works quite well for uniform sediments with diameters $>100 \mu\text{m}$ for which the interparticle cohesion is negligible. However, this model offers less explanatory power for smaller particles and for natural sediments that contain a mixture of grain sizes and shapes that also vary in grain density and packing. Shape may play a more important role in influencing u_{*t} for volcanic ash than mineral grains derived from the weathering of rock, because ash particles range widely from rounded grains of varying crystallinity to crystal-free concavo-convex particles (Liu et al., 2014). Particles that are irregular in form have been observed to have lower threshold values than spherical particles of equivalent mass (Goldasteh et al., 2012; Willetts et al., 1982; Williams, 1964).

The force-balance theory of threshold has been advanced through time as the physical controls on the process are better understood. Shao and Lu (2000) derived an expression for u_{*t} that considers particles with a cohesion force that is proportional to particle size

$$u_{*t} = \sqrt{0.0123 \left(\frac{\rho_p g d}{\rho_a} + \frac{\gamma}{\rho_a d} \right)}, \quad (3)$$

where ρ_p is particle density (kg/m^3), g is acceleration due to gravity (m/s^2), and γ is a cohesion parameter between 1.65×10^{-4} and $5 \times 10^{-4} \text{ kg/s}^2$. The least quantified of the parameters in equation (3) is γ that represents the role of cohesion, which is not easily measured and for which values are not available from a database. This equation was used by Folch et al. (2014) to model the u_{*t} of ash from deposits associated with the June 2011 Cordón Caulle eruption in central Patagonia, Argentina, assuming that $\gamma = 3 \times 10^{-4} \text{ kg/s}^2$, which is approximately midway between Shao and Lu's (2000) reported range and provides an estimate for u_{*t} of 0.25 m/s. As most mineral particles in earth material sediment approximate spheres, the effect of particle shape on influencing threshold has not been incorporated into equations for estimating u_{*t} .

2.1.2. Effect of Moisture and Crusting on Threshold

The presence of moisture provides a critical control on threshold in terms of the moisture content of the sediment matrix as well as the moisture in the atmosphere. Early research efforts by Belly (1964) demonstrated that gravimetric moisture content dramatically affects u_{*t} . Expressions have been developed, mostly by empirical means, to account for the effect of pore water in the sediments to affect u_{*t} (e.g., McKenna Neuman & Nickling, 1989). The expression derived by Fécan et al. (1999) to characterize the effect of moisture content on u_{*t} has become popular for use in wind erosion models (e.g., Marticorena, 2014; Minvielle et al., 2003; Munkhtsetseg et al., 2016) because it is easy to estimate from available data. Using this correction scheme for moisture effects on u_{*t} , Folch et al. (2014) estimated u_{*t} to be 0.4 m/s for the Patagonian ash resuspension event they reported on. This value was also reported by Leadbetter et al. (2012) as the u_{*t} for resuspension of Eyjafjallajökull ash deposits in Iceland.

A second moisture effect on u_{*t} is linked with the relative humidity (RH) of the air above a dry, erodible surface (McKenna Neuman, 2003, 2004; McKenna Neuman & Sanderson, 2008; Ravi et al., 2004, 2006). In a series of wind tunnel experiments McKenna Neuman and Sanderson (2008) demonstrated that fine particles, particularly those that are tightly packed, in a dry condition are most affected by changes in RH. Their data show that for nonpore water (i.e., adsorbed water films), the increase in u_{*t} with increasing RH is dependent on the number of contacts between the particles, which increases rapidly as adsorbed water films grow in response to increasing RH. Ravi and D'Odorico (2005) present field data that show that u_{*t} at their study site was significantly dependent on atmospheric RH, but this effect was observed to reach a well-defined, local maximum at $\text{RH} \approx 35\text{--}40\%$ for air-dry soils after which the threshold once again decreases. As the contact areas of the adsorbed films merge under even higher humidity (nominally $>65\%$), liquid pore water may

begin to form within the soil matrix and the threshold may begin to increase again as the regime changes to one where pore water in the sediment provides binding between particles.

Del Bello et al. (2018) reported on a series of laboratory-based measurements of u_{*t} for ash samples from the Campi Flegrei region of Italy and Eyjafjallajökull in Iceland. They found that u_{*t} was sensitive to RH, especially when RH was higher than 90% and when the particles considered were smaller than 63 μm (obtained by sieving). In an intermediate range of RH (50–70%), particles smaller than 63 μm exhibited u_{*t} values from 0.35 to 0.45 m/s. Coarser particles (63–125 and 125–250 μm) had lower values of u_{*t} (0.2–0.3 m/s) that were much less impacted by changes in RH.

The presence of a surface crust on soils, in the absence of disturbance, has been observed to create a condition that is highly resistive to wind erosion. The efficacy of the binding forces associated with bonding agents, such as clays or salts, to affect wind erosion threshold and dust emission rates has been clearly demonstrated. The effectiveness of clay minerals to act as bonding agents depends on their relative proportion in relation to the sand-sized particles in the sediment. The presence of soluble salts also greatly affects wind erosion thresholds (Gillette et al., 1980, 1982; Nickling, 1978; Nickling & Ecclestone, 1981). The crust strength will be dependent on the texture of the sediment, the type and characteristics of the mineral bridges (clay or salt minerals) between particles, the antecedent moisture conditions (Holcombe et al., 1997), and disturbance history (Houser & Nickling, 2001a).

2.1.3. Emissions Magnitudes

It is generally recognized in the mineral dust emission literature that the mobilization of sand-sized particles by wind, which move in ballistic trajectories (i.e., saltation) and repeatedly impact the surface, is often a leading cause of significant emissions of the smaller dust-sized particles (<50- μm diameter). This has been termed the sand blasting model of dust emissions (Gomes et al., 1990).

From dimensional analysis, Gillette and Stockton (1986) showed that the kinetic energy flux of saltation is proportional to u_*^3 , which Gillette et al. (2004) reason is absorbed and carried to the surface by saltating particles. Martin and Kok (2017) have recently reevaluated this relationship, and their detailed field measurements of the saltation process suggest that saltation flux is proportional to u_*^2 . It then follows that the vertical kinetic energy flux associated with the saltating particles is also proportional to u_*^3 or u_*^2 . Shao et al. (1993) developed a dust emission model that is based on defining the relationship between emissions and the abrasive force associated with the kinetic energy of the saltating particles and the resistive or bond strength of the sediments being impacted ballistically. Field measurements of dust emissions (F) show that the theoretically derived power function, which can be expressed as

$$F \propto u_*^n, \quad (4)$$

is not universal, with the empirically fitted exponent n having been reported to span between 1.89 and 6.2 (Ishizuka et al., 2014).

The capability of wind shear or a saltating sand particle to cause the emission of dust or ash depends on the proportion of energy available to break interparticle bonds relative to the resistance of those bonds to rupturing. The resistance to the release of a dust-sized particle from sediment being acted upon by the forces of the wind and the ballistic impact forces of saltating particles can be characterized by what Shao et al. (1993) introduced as the binding energy term, ψ . These binding energies scale with particle size, moisture content, and the strength of the crust that can form in the sediment.

Disturbance of a surface can both increase the probability that emissions will occur and increase the magnitude of emissions from that surface. The increase in the probability of emissions is a result of lowering u_{*t} , making the surface more susceptible (e.g., Belnap & Gillette, 1997). The strength of dust emissions is related principally to the particle size distribution of the sediments (i.e., soil texture), soil moisture content, salt and clay mineral bond strengths, and the roughness of the surface. Disturbance can alter or modify these properties to various levels of severity. Emission is also influenced by supply limitations of the freely available dust- and sand-sized particles. If disturbance releases sand from the sediments—which relaxes the supply limitation—and the threshold is subsequently reached, particles are available to saltate and impact the surface, which releases dust particles in proportion to the sum of the resistive forces and as a function of the integrity of the surface (Gordon & McKenna Neuman, 2009; Houser & Nickling, 2001b).

Although disturbing surfaces susceptible to dust emissions create a complex interplay between the driving and resisting forces, in general, there is an increase in particle emission rates, and therefore, the same effect would be expected for deposited ash. Based on the available evidence from the literature, disturbance increases emissions by approximately 1 order of magnitude compared with the rate of the undisturbed condition (Gillies, 2013). For more sensitive sediment systems that are rich in dust-sized particles, which may be the case for deposited ash, the potential for increases above 1 order of magnitude is plausible.

In addition to the resistive forces that operate chiefly by binding particles together at the grain scale, other physical properties of the surface affect the emission process. Primary among these is the scale of the surface roughness. Roughness effects can be aerodynamic and physical. Aerodynamic effects arise from the flow properties that are influenced by the degree or scale of the roughness (Raupach et al., 1993; Shao & Yang, 2008). Physical effects are related to the interaction of the moving sediment with the roughness (Gillies et al., 2018; Gillies & Lancaster, 2013; Wolfe & Nickling, 1993). As this laboratory-based study only tested surfaces in the absence of large roughness elements, we will not address the effects of superposed roughness on ash resuspension and emission rates but recognize that this may be an important aspect to consider for real-world conditions.

2.2. Resuspension of Volcanic Ash

The resuspension of volcanic ash is known to actively occur in many parts of the world. As early as 1933, reports of “brown snow” reported across Canada and the northern United States (Alexander, 1934; Miller, 1934) were ultimately attributed to the remobilization of the extensive volcanogenic material produced by the 1912 eruption of Novarupta (Hildreth & Fierstein, 2012). This material has remained an active source of resuspendable ash: Hadley et al. (2004) reported ash plumes disrupting air transport in 2003 and Webley (2013) described an ash plume that traveled southeast from the Katmai area across the Gulf of Alaska in May 2013. These events continue to the present day.

Resuspension events are observed to occur immediately after the deposition of ash, as well as recurrently for months, years, decades, and centuries after deposition. Multiple resuspension events following eruptions have been observed by Hobbs et al. (1983) for MSH, Wilson et al. (2011) for Mount Hudson in Chile, Barsotti et al. (2010) for Mount Etna in Italy, Folch et al. (2014) for Puyehue-Cordón Caulle in Chile, and subsequent to the eruption of Eyjafjallajökull in Iceland (e.g., Dagsson-Waldhauserova et al., 2013; Leadbetter et al., 2012; Liu et al., 2014). Mingari et al. (2017) report on a resuspension event in the Fiambalá Basin, Argentina, originating from ancient pyroclastic deposits of the Cerro Blanco eruption that occurred circa 4.5 kyr before present.

Some research has been reported on the resuspension of MSH 1980 ash. Fowler and Lopushinsky (1986) estimated from wind tunnel testing of loose dry ash collected from the 1980 eruption that a smooth surface of ash particles was suspendable at a wind speed of ≈ 3 m/s, and surfaces with small mounds of ash spaced irregularly were suspendable at even lower speeds of 2–2.5 m/s. According to Fowler and Lopushinsky (1986), material smaller than 3.5- μm diameter was most susceptible to entrainment. Following the wetting of the ash samples and the subsequent air drying, the ash could not be resuspended by winds up to ≈ 20 m/s. Disturbing the wetted/dried ash decreased the threshold wind speed to ≈ 6 m/s.

Sehmel (1982) reported a monthly average threshold wind speed for resuspension of MSH ash in the vicinity of the Hanford Site of 3.6 m/s, but he concluded that this was potentially biased as it likely represented material that was resuspended upwind of the Hanford Site for wind speeds that differed from those measured at the Hanford Site (i.e., the wind speed measured and the wind speed that caused upwind resuspension were not the same). Sehmel (1982) also observed that resuspension was suppressed following precipitation events. He noted that from May to July 1980, 0.5–1.5 cm of rain was required to significantly reduce airborne concentrations of particles associated with winds that had previously resulted in particle concentration increases. After the passage of more time (5 months), additional rainfall of 2.0 cm had a negligible effect on particulate matter levels.

These threshold wind speeds for resuspension can be converted to u_{*t} by making a few assumptions. Unfortunately, Sehmel (1982) does not provide the height above ground level (AGL) of the wind speed measurements, and the aerodynamic roughness (z_0) of the surface is unknown. Assuming that the height of the wind speed measurement is 10 m (standard meteorological measurement height) or 3 m (the likely height of

the particulate matter measurements) and a smooth aerodynamic roughness of 0.001 m, an intermediate value of 0.01 m, and a rough value of 0.10 m, application of the Prandtl (1935) relationship describing the wind profile close to the surface

$$\frac{u_z}{u_*} = \frac{1}{\kappa} \ln\left(\frac{z}{z_0}\right), \quad (5)$$

where u_z is the horizontal wind speed at height z and κ is von Kármán's constant (0.4), provides estimates of u_{*t} from 0.13 m/s ($z = 10$ m, $z_0 = 0.001$ m) to 0.35 m/s ($z = 3$ m, $z_0 = 0.10$ m). This is a wide range because of the ambiguity in how wind speed was measured, which was not detailed by Sehmel (1982). Based on particle size measurements of deposited ash at Richland and Yakima, WA, Hobbs et al. (1983) applied Bagnold's (1941) relationship between particle diameter and u_{*t} to arrive at values of 0.8 m/s for 1,000- μm particles and 0.1 m/s for 10- to 20- μm particles at Richland. Using the Bagnold (1941) relationship for the mean particle diameter of 33.6 μm that was reported by Durant et al. (2009) and a mean particle density of 0.99 g/cm³ (Moen & McLucas, 1981) for particles deposited between 160 and 282 km downwind, u_{*t} would be 0.19 m/s.

2.3. Ash Properties and Entrainment and Transport in Suspension

The entrainment potential of volcanic ash by wind varies widely, and no doubt reflects the wide range in deposit properties. Suspendable deposits contain abundant fine ash. A convenient definition of fine ash is <63 μm —the finest diameter that can be easily measured in sieve analyses. The fraction of ash <63 μm produced during a single eruption can range from less than a few percent in basaltic eruptions (Scollo et al., 2007) to more than 80% in some dome collapse events (Bonadonna et al., 2002). In general, fine ash is more abundant in larger eruptions, or those in which pyroclastic flows were abundant (Darteville et al., 2002). Within a single deposit, fine ash increases in abundance with downwind distance, though some fine ash is present at nearly all distances. In the 1980 MSH deposit, for example, the percentage of ash ≤ 63 μm in diameter increased along the dispersal axis from about 43% to 48%, 81%, and 92% as distance increased from 98 to 154, 248, and 422 km, respectively (Durant et al., 2009).

Particle entrainment and its subsequent transport in suspension also depend on shape and density of each particle. Mineral fragments are denser, more equant, and likely harder to suspend than light, irregularly shaped pumice. In magmatic eruptions, the fraction of erupted debris consisting of mineral fragments ranges from less than a few percent (Bacon & Lanphere, 2006; Castro & Dingwell, 2009) to several tens of percent (Gardner et al., 1998). Mineral phenocrysts are most often millimeter sized and tend to fall proximally (because of their density) or at distances governed by their characteristic size. Distal deposits are richer in glassy bubble walls, whose size can range down to microns.

Within this spectrum, one might expect resuspension to be most important in medial to distal areas where fine ash is abundant and deposits are thick enough to provide a persistent source. Proximal deposits, like the VTTS, can suspend ash for many decades as well.

3. Experimental Methods

The laboratory experiments were designed to quantify resuspension of ash deposits on relatively smooth terrain. In summary, we sampled natural volcanic ash from MSH and VTTS, prepared it in the lab to replicate field characteristics (realistic bulk densities in the range of 1,300–1,500 kg/m³), and subjected the deposits to varying wind speeds and levels of humidity. We used the PI-SWERL® instrument (Etyemezian et al., 2007, 2014; Sweeney et al., 2008) in a controlled-environment chamber (temperature and humidity) to measure threshold wind conditions for particle resuspension and emission rates as a function of surface shear stress (see equation (2)).

3.1. Volcanic Ash Sampling and Characterization

To obtain natural volcanic ash for our experiments, we focused on thick, proximal deposits from MSH and VTTS where we could collect large amounts (~1,000 kg) of relatively homogeneous material. Deposits were collected in the field in 2016 and returned to the lab for characterization by scanning electron microscopy, sieving, and laser diffraction particle size analysis.



Figure 1. Location map of MSH sample site (left) and source of volcanic ash from deposits of dilute pyroclastic density currents on the afternoon of 18 May 1980, showing MSH in the background (right). MSH = Mount St. Helens.

3.1.1. Sampling Site at MSH, Washington

Roughly 1,000 kg of bulk deposit was sampled ~8 km north of MSH, from an area known locally as the “ramp” (46.26957°N, 122.18092°W). Here, the 1980 deposits are fine grained, locally >1–2 m thick, and were emplaced as multiple, dilute pyroclastic density currents on the afternoon of 18 May 1980 (Phases III–IV of Criswell (1987)). Water erosion of the deposits since 1980 has produced Badlands-type topography with outcrops along gully margins 1–2 m high. Samples were collected from a gully margin using shovels and placed into six, 110-liter steel drums with lids on 20 July 2016 (Figure 1). The drums were removed by helicopter and then transported to the Desert Research Institute facility in Las Vegas, Nevada.

The deposit offered several desirable characteristics for this study. First, being from the 1980 eruption, it provides a reasonable approximation of future eruption deposits from MSH. Second, the material is volumetrically abundant and pristine (relatively unaltered glass that has not been reworked/mixed with other sediments after deposition). By contrast, the MSH 1980 fall deposits farther downwind are thin and mostly reworked, which would be difficult to sample in large quantities and would probably include foreign particles. Third, the material is relatively homogenous and fine grained (<1 mm), providing consistent textural properties for our experiments.

3.1.2. Sampling Sites in the VTTS, Alaska

From the VTTS, we sampled ≈1,000 kg of pyroclastic density current and fall deposits from the 1912 Novarupta eruption (Fierstein & Hildreth, 1992). The material originates from the 6–8 June 1912 eruption of Novarupta caldera, the largest eruption of the twentieth Century (Hildreth & Fierstein, 2012). We sampled two main sites between 6 and 20 km from the caldera on 26–28 July 2016 (Figure 2). At each location, shovels were used to clear the surface layer of larger nonwind erodible particles and sample the upper ≈3 cm into 30-gallon steel drums with lids. Samples VTTS 1 and 2 were collected from beneath a lag deposit on a shelf NW of the Ukak River (58.40151°N, 155.38569°W) and displayed a color (pinkish), poor sorting, and maximum size of decimeters that suggested them to be the upper part of the ignimbrite, perhaps Package 4 of Fierstein and Wilson (2005). Samples VTTS 5 and 6 were collected 300 m west of Knife Creek in midvalley (58.35327°N, 155.30924°W), from beneath a lag deposit of similar size that may represent a remnant of ignimbrite Packages 4, 5, or 6 based on location (Fierstein & Wilson, 2005). Overall, six barrels of ash were transported from the VTTS by helicopter back to King Salmon, Alaska, and shipped to the Desert Research Institute in Las Vegas, Nevada.

VTTS was chosen because it offered an abundant source of material with different characteristics from MSH (coarser grain size, more crystal rich), allowing the experiments to capture a range of deposit types. Furthermore, VTTS continues to be a source of active resuspension (Alexander, 1934; Hadley et al., 2004; Schwaiger & Wallace, 2015), often affecting regional air quality and local aviation (Hadley et al., 2004).

3.2. Particle Characterization: Scanning Electron Microscopy (SEM) and Grain Size Analysis

Samples were prepared for grain size analysis by lightly crushing the bulk sample with a mortar and rubber-tipped pestle to gently break up clusters. The material was dry sieved to 1 mm. For particles <1 mm, we used

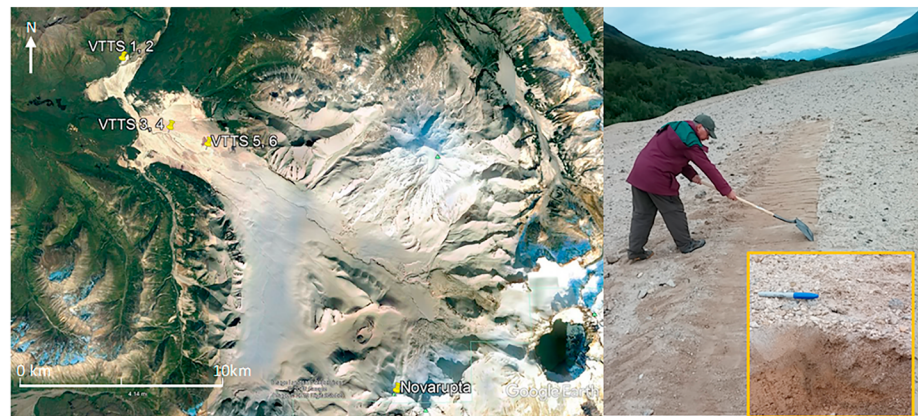


Figure 2. Location of VTTS sample sites (Left) and photograph of Site 1 (Right) with crusted surface (Right, inset). VTTS = Valley of Ten Thousand Smokes.

a Beckman Coulter LS 13 320 laser diffraction particle size analyzer. Laser diffraction analyses were repeated three times (60 s each) to obtain an average distribution for each sample. Because the MSH and VTTS deposits are both dacitic in composition, we used a single optical model—values of 1.5 for the real refractive index and 0.0005 for the absorption coefficient, based on comparison with published studies (Ball et al., 2015) and the ISO lookup table (ISO, 2009). Laser diffraction measures the volume percent in each size class (rather than weight percent like sieving), but results are comparable if a constant particle density is assumed. Therefore, to combine results from the two methods, we simply multiplied the laser data by the fraction of ash >1 mm in the whole sample measured by sieving.

3.3. Sample Preparation

Ash samples from VTTS and MSH were oven dried at 250 °C for 8 hr. Then subsamples were placed into eight custom-built sample boxes, which were constructed of plywood (1.0 m [L] \times 1.0 m [W] \times 0.14 m [H]) (Figure 3).

The inside of each sample box was lined with aluminum sheeting to minimize air and moisture exchange through the sides and bottom. At the center of each box, along the bottom surface, a metal electrical junction box (4 cm per side by 2-cm depth) was mounted atop the aluminum sheeting. An electronic temperature and RH sensor was emplaced within the junction box. The junction box, which had several holes (\approx 1-cm diameter) on each of the four sides, was covered in plastic screening to keep out ash material but allowed the free flow of air into and out of the junction box and embedded temperature/RH sensor. Electrical wires that were run from the junction box to a connector on the outside of the sample holder box served as communication lines for the temperature/RH sensor as well as to electrically ground the junction box and the aluminum sheeting inside of the sample box. Each sample box was large enough to allow up to four PI-SWERL tests to be conducted without overlap.

Four sample boxes were filled to a depth of 0.08 m with MSH ash, three were filled with VTTS ash (one each with VTTS1, VTTS2, and VTTS5), and one was filled with sand that was collected from the Oceano Dunes, which are located along the Central Coast of California, USA. The dune sand was included in the sample mix because of substantial prior in situ measurement of wind erosion characteristics of this source using the PI-SWERL (Etyemezian et al., 2014), which would allow for a comparison/control for the ash samples, with which we had no prior experience. The material in each test box was evenly distributed within



Figure 3. Stack of aluminum-lined sample holders inside sample conditioning chamber. Orange device is a hydraulic forklift used to maneuver sample holders within chamber. Temperature and relative humidity sensors were buried at the center and bottom of each sample holder box (not visible).

the box using a garden rake and then levelled with a straight edge to remove the ridges created by manipulation with the rake creating a relatively smooth surface. None of the samples was sieved or intentionally disaggregated before loading into the sample boxes.

3.4. Sample Conditioning

Prior to undergoing PI-SWERL testing, the samples in the boxes underwent conditioning within an environmental chamber (4 m [L] × 3 m [W] × 2 m [H]) by maintaining the air temperature and RH within the chamber at values set by the user. The chamber was constructed of interlocking, thermally insulated aluminum panels. The edges between adjacent panels were taped to improve insulation. A door (0.9 m × 1.9 m) was the only entry and exit point from the lab to the chamber.

The temperature and RH within the chamber were monitored by sensors at three locations to ensure uniformity, but only one sensor (main) was used to control the two parameters within the chamber. The nominal temperature set point for all tests was 29 °C. This temperature was chosen because it allowed for achieving all of the RH set points inside the chamber without having to actively cool the chamber (which would introduce problems related to condensation) given that the temperature of the laboratory housing the chamber was generally regulated by the building HVAC at 22 °C. The temperature in the chamber was brought to its set point using two electric heaters located on opposite walls within the chamber. Humidity was added as needed by bubbling air through a heated deionized water bath that was located within the chamber. When needed, humidity was lowered by circulating chamber air through a drying capsule that contained 10 kg of molecular sieve material. A second capsule was available so that the molecular sieve material from one capsule could be oven regenerated, while the other capsule was used to remove moisture from the chamber. A fan was used to constantly circulate air within the chamber and through the gaps between the sample boxes so that the temperature and RH within the chamber and immediately above the test surfaces were essentially uniform.

An air filtration system was installed to actively remove suspended particles from the chamber air. The filtration system consisted of an electric vacuum that was fitted with a HEPA rated filter. The vacuum end was attached to a shroud that was hung from the ceiling. The exhaust from the HEPA filter was routed through a perforated manifold along one wall of the chamber so that filtered air was introduced diffusely over the length of the chamber. The air filtration system was used in two ways. First, it served to remove suspended dust from within the chamber by effectively filtering the air in order to keep airborne particle concentrations at a manageable level. Second, it served as a dilution device for PI-SWERL suspended ash as described in the next section.

All electronic instruments within the chamber were connected to a central data logging and control computer that recorded data at 5-s intervals and also controlled the operation of the water bath heater, water bubbler, molecular sieve dryer pump, the wall heater units, and the air filtration system.

3.5. Ash Particulate Matter Threshold and Emissivity Testing

Particle entrainment threshold shear velocity, u_{*t} (m/s), and particle emission flux, F ($\text{mg}\cdot\text{m}^{-2}\cdot\text{s}^{-1}$) were determined using the PI-SWERL instrument (Etyemezian et al., 2007, 2014) (Figure 4). Briefly, the PI-SWERL consists of a cylindrical chamber (0.30-m diameter) that is open on one end. The open end is placed on top of the test surface and is sealed against the surface with elastomeric foam. An annular blade is suspended from the top cylinder approximately 0.05 m above the test surface and connected to a motor at the top of the cylindrical chamber, which is controlled through software interface. When the motor spins the blade, shear stress is created on the test surface (Etyemezian et al., 2014) by the rotation of the annular blade. Clean air is injected into the cylinder at a flow rate of 100 liters per minute (lpm); it mixes with the dusty air inside and then it is exhausted out of a port at the top of the chamber. A small port at the top of the chamber is connected to a dust monitor (DustTrak 8530, TSI, Inc.) so that the concentrations of particulate matter within the chamber are measured once per second. The dust monitor is equipped with a size cut device so that it measures particles $\leq 10\text{-}\mu\text{m}$ aerodynamic diameter (PM_{10}).

Two types of test programs were used in each testing cycle, the “Ramp 3000” test to determine u_{*t} and the “Hybrid 3500” test for developing the emission flux relationship: $F = u_*^n$. The Ramp 3000 cycle (Figure 5) begins with a 60-s clean air flush in which the clean air blower is operating, but the annular blade is still

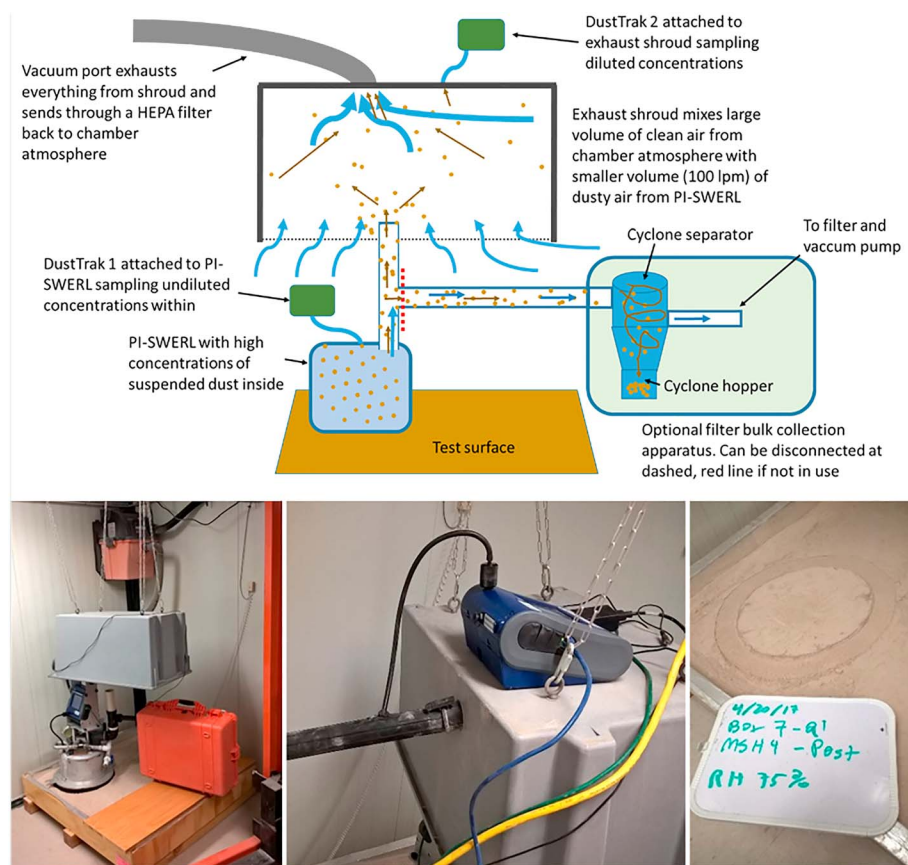


Figure 4. (top) Flow schematic for PI-SWERL dilution tests. Blue arrows schematically represent flow of air, and brown arrows schematically represent flow of particles. (bottom left) PI-SWERL on Q1 test quadrant with exhaust shroud (gray). The orange box was used to collect bulk suspended material for size analysis in a subset of tests. (bottom middle) Placement of second DustTrak and sample line connection into exhaust filtration duct. (bottom right) Example photograph at the end of (post) testing of Box 7 at 75% RH showing the area tested with the PI-SWERL (inside circular pattern above white board). RH = relative humidity.

so that particles that may have become suspended within the chamber during the placement of the PI-SWERL on the test surface are flushed out. Thereafter, the annular blade rotation is linearly increased from 0 revolution per minute (RPM) to 3,000 RPM over the course of six minutes (500 RPM/minute). Once the rate of rotation reaches 3,000 RPM or the operator stops the test, power to the blade is cut and clean air is flushed through the chamber for 90 s to clear out particles suspended within.

For the Hybrid 3500 program (Figure 6), 60 s of clean air flush is followed by an increase of the blade rotation from 0 to 1,500 RPM over the course of 60 s (1,500 RPM/minute). The rotation rate of 1,500 RPM is held constant for 90 s, followed by an increase in rotation to 2,000 RPM over 60 s (500 RPM/minute). The rotation rate is held at 2,000 RPM for 90 s before it is increased to 2,500 RPM over 60 s (500 RPM/minute). This is repeated until the rotation rate is 3,500 RPM or the operator stops the cycle at which time the power to the blade is cut and the cylindrical chamber is flushed for 90 s.

Resuspended ash was collected from the PI-SWERL exhaust manifold for analysis of its particle size characteristics. This was accomplished with a Very Sharp Cut Cyclone (VSCC; Kenny et al., 2000) particulate matter sampler (Figure 4). A battery operated pump and mass flow controller aspirated 16.7 lpm, the design flowrate for the VSCC, out of the PI-SWERL exhaust through the inlet line of the apparatus. When in use, the sampler was configured to turn on at the beginning of the PI-SWERL test and automatically turn off at the end. It was used to collect VTTS resuspended material over multiple PI-SWERL tests. Subsequently, the hopper was emptied into a labeled container. The sampler was then used over multiple PI-SWERL tests to collect resuspended MSH material into the hopper.

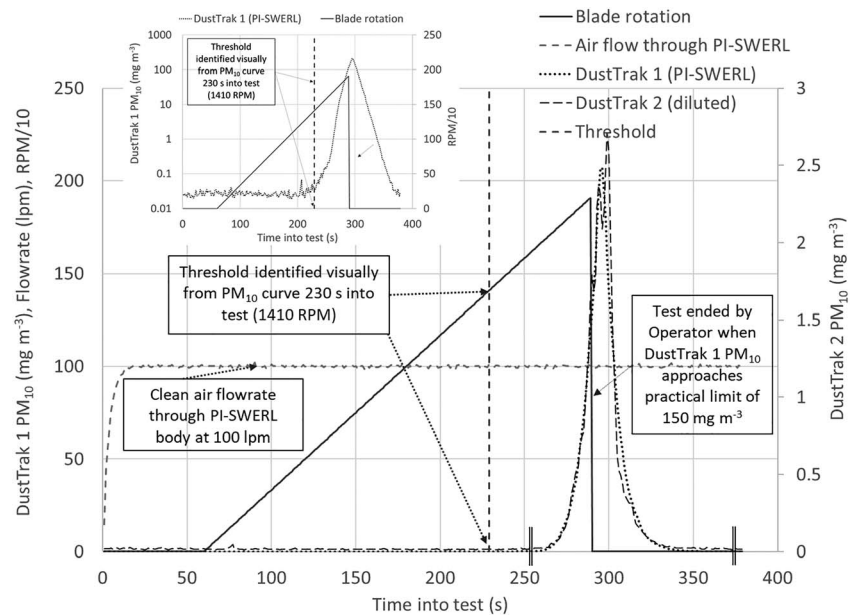


Figure 5. Example PI-SWERL ramp test used for estimation of threshold for emissions and scaling of PI-SWERL and dilution DustTrak instruments. Because of linear scaling of the y axis, it is difficult to see that at 230 s into the test, the PM_{10} concentrations begin to rise consistently in response to the blade rotation (i.e., threshold had been achieved). Inset shows the DustTrak 1 signal on a log scale which makes threshold easier to identify.

It is important to note that, due to the rotational nature of the flow within the cylinder, the PI-SWERL behaves somewhat like a cyclone separator. This has the effect of imposing an effective size cutoff on the particles that are entrained within the PI-SWERL chamber; smaller particles follow the airflow out of the instrument while larger particles stay inside the chamber. Although systematic measurements have not been conducted to characterize this effect, it is expected that the cyclonic effect begins affecting particles' ability to leave the PI-SWERL starting with particles at around $5 \mu m$ in diameter; the effect increases with particle size so that particles larger than $20 \mu m$ in diameter are severely restricted from leaving (we estimate coarsely 5–30% success rate) the PI-SWERL through the exhaust port and particles larger than $80 \mu m$ are unable to

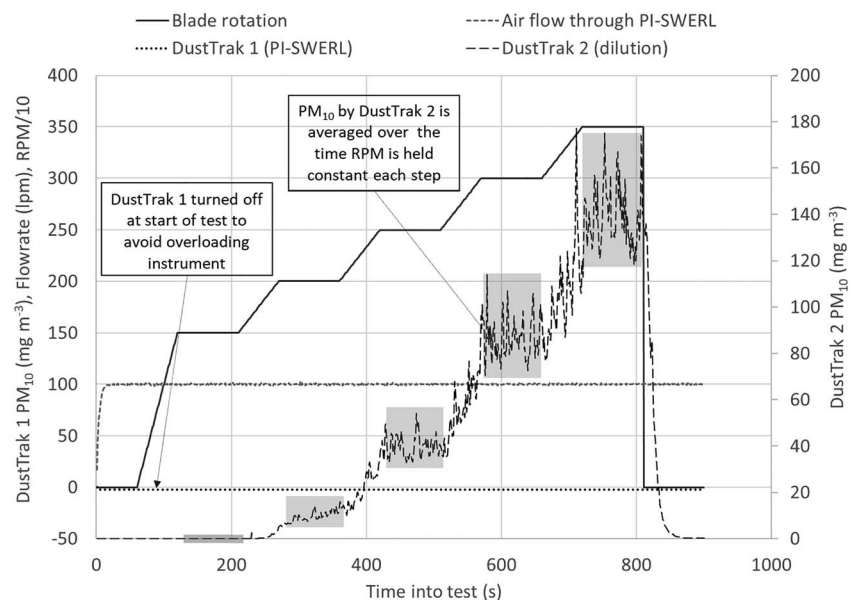


Figure 6. Example estimation of PM_{10} emissions at varying levels of u^* . Gray-shaded regions indicate periods when averages of PM_{10} concentrations were calculated. PM = particulate matter; RPM = revolution per minute.

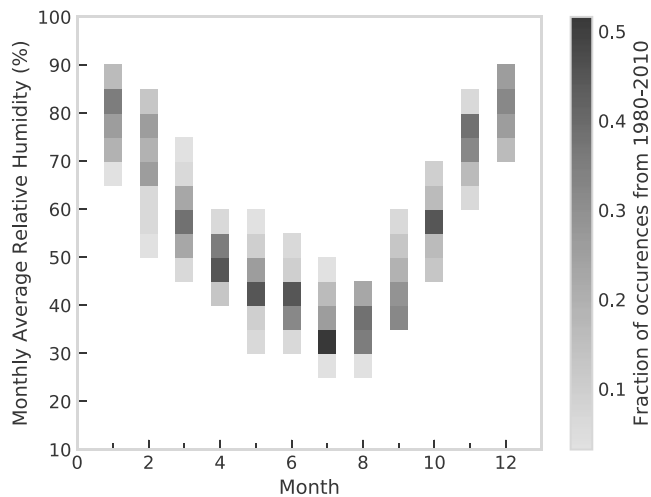


Figure 7. Monthly average relative humidity for each of the 30 years between 1980 and 2010 at the Hanford Washington Station (46.57°N and 119.6°W) as calculated from surface observations of temperature and dew point derived from the Integrated Surface Database (Smith et al., 2011).

exit the PI-SWERL chamber altogether. When the cyclonic effect of the PI-SWERL is considered in combination with the effect of the VSCC cyclone, we expect that size distribution analyses conducted on material collected in the hopper underrepresent particles smaller than 2.5 μm and particles larger than about 20 μm .

In-lab PI-SWERL testing occurred during three time periods. The first testing period was between 15 March 2017 and 28 April 2017. Samples were conditioned in the environmental chamber until the embedded temperature and RH sensor indicated that the sample temperature had not changed more than 1 °C and that the RH had not changed more than 5% in the prior 24 hr. When a sample box was undergoing PI-SWERL testing, it was moved to the area of the chamber near the air filtration instrumentation. The PI-SWERL was placed on one of the four quadrants of the test box that had not undergone previous testing (To avoid repeated testing, sample material was reraked and releveled approximately every three test dates). The exhaust shroud was moved atop the PI-SWERL exhaust (Figure 4) prior to commencing tests. Each sample box was tested once, and two sample boxes were chosen at random for replicate testing on a quadrant that had not undergone previous testing. Following the completion of PI-SWERL testing, the sample box was replaced on the condition-

ing stack and another box was selected for testing. Photographs were obtained prior to and after testing of each box (Figure 4) to document the appearance of the surface.

During this first testing period, it was discovered that dust concentrations measured in the PI-SWERL chamber were much higher than anticipated and would frequently exceed the measurement range of the DustTrak instrument, in some cases very early during a test. These tests were conducted at nominal RH settings of 15%, 25%, 50%, 75%, and 90%. The intent was to obtain measurements over the entire range of RH levels that are encountered over the course of a typical year (Figure 7). Note that the RH can vary considerably over the course of 1 day or even a few hours. However, ash on the ground would require several hours to days to react to dramatic changes in RH, so that it is appropriate to consider longer-term averages of ambient RH in determining an appropriate range for ash resuspension testing.

The tests conducted during this first period were useful for collecting information on u_{*t} and its relationships with bulk density and soil moisture in response to changes in RH. However, estimates of PM_{10} emissions from these tests are not reported because of the large temporal gaps in the DustTrak data (due to instrument overranging). The experience of testing during the first period prompted a revision of the testing procedures for acquisition of data to generate the emission rate data.



Figure 8. (left panel) Application of water prior to third testing period. (right panel) Masonry block atop wetted surface to simulate light compression.

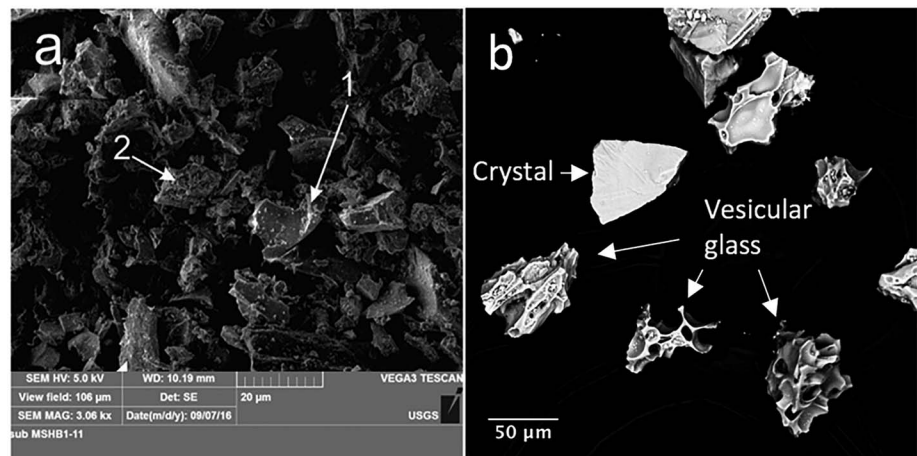


Figure 9. Scanning electron micrographs of MSH volcanic ash used in experiments. (a) Bulk, unwashed sample shows fresh glass with adhering fines (1) and precipitates coating some surfaces (2). (b) Washed, sieved sample shows unaltered, vesicular glass and crystals. Images are from sample MSHB1. MSH = Mount St. Helens.

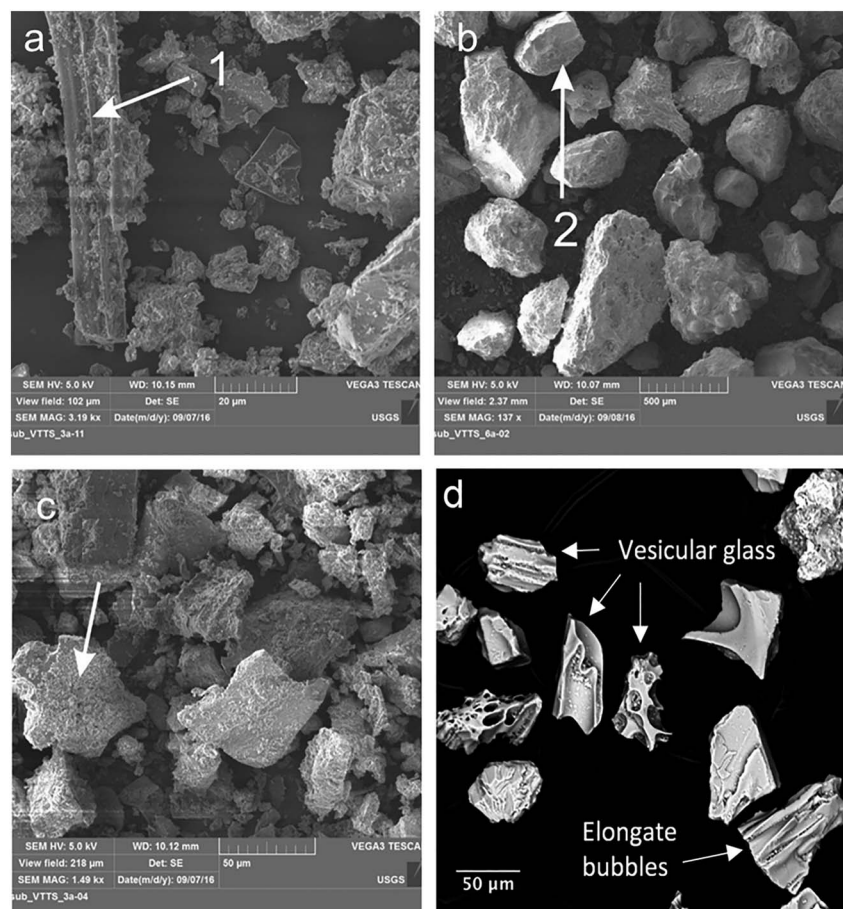


Figure 10. Scanning electron micrographs of fragments bulk, unwashed particles from VTTS ash used in experiments, sourced from (a) VTTS3, showing adhering fines; (b) VTTS1, pointing out a crystal; and (c) VTTS3, showing a surface with alteration and/or precipitate coating. (d) Washed, sieved particles from VTTS2a, highlighting vesicular glass, including some with elongate bubbles. VTTS = Valley of Ten Thousand Smokes.

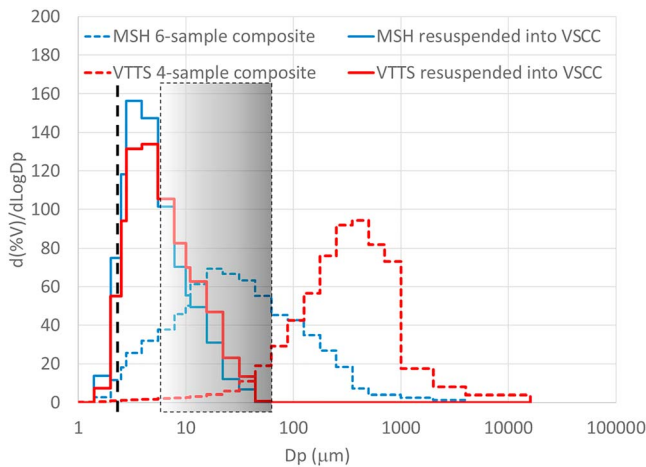


Figure 11. Particle size distributions of bulk ash from VTTS and MSH and resuspended ash from PI-SWERL experiments. For the resuspended ash, note that particles $<2.5 \mu\text{m}$ $> 5\text{--}80 \mu\text{m}$ were preferentially removed by processes in the system and are therefore underrepresented in these data. However, there is a nonnegligible proportion of resuspended particles larger than $10 \mu\text{m}$. Vertical black line shows the lower size limit of resuspended particles that could be sampled ($2.5 \mu\text{m}$). Shaded gray box represents the increasingly efficient removal of ash $5\text{--}80 \mu\text{m}$ by cyclonic action of the PI-SWERL instrument. MSH = Mount St. Helens; VTTS = Valley of Ten Thousand Smokes; VSCC = Very Sharp Cut Cyclone.

Following the two Ramp 3000 tests, two Hybrid 3500 tests were executed. In these tests, DustTrak 1 was turned off very early in the test (first few seconds) to avoid overloading the instrument unnecessarily. Using data from DustTrak 2, average PM_{10} concentrations in the dilution line were calculated over periods of constant RPM (see Figure 6). The dilution correction multiplier was then used to estimate PM_{10} concentrations inside the PI-SWERL chamber (multiplier of 88.5 in the example shown in Figure 6 based on the preceding two Ramp 3000 tests in the test cycle). These were then used to estimate PM_{10} emission factors (EF_{10} , $\text{mg}\cdot\text{m}^{-2}\cdot\text{s}^{-1}$) at specific RPM values

$$EF_{10,i} = \frac{C_{\text{PM}_{10,i}} \cdot FR \cdot 0.0000167}{A_{\text{eff}}}, \quad (6)$$

where $C_{\text{PM}_{10,i}}$ refers to the average concentration of PM_{10} inside the PI-SWERL chamber over the duration of step i , FR is the flow rate through the chamber in liters per minute (100 lpm for all tests reported here), the constant multiplier is a unit conversion adjustment, and A_{eff} is the PI-SWERL effective area (Etyemezian et al., 2014).

The second testing period was intended to elucidate the major effects of ambient RH on the PM_{10} emissions. Testing was conducted on samples conditioned at a temperature of 29°C and RH values of 50% (6/7/17), 25% (6/14/17), and 75% (6/19/17). The range of RH conditions tested was reduced during the second testing period as compared to the first but still covered most of the range of conditions that are likely to be encountered at Hanford (Figure 7).

The third testing period was intended to elucidate the effect of wetting and surface crust formation on particle emissions. On 29 September 2017, deionized water was applied to all sample boxes with a hand sprayer (Figure 8) to provide water equal to 5 mm of precipitation. The volume was added incrementally over the course of more than 100 sweeps

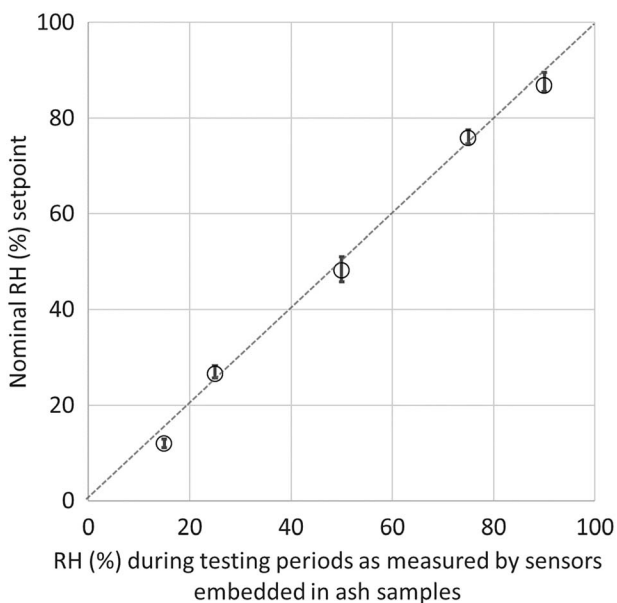


Figure 12. Averages of RH from embedded sensors and indicated nominal RH set points in the environmental chamber. Data shown are for tests prior to application of liquid water. Vertical bars represent minimum and maximum individual sample averages. Temperature in chamber and test boxes was constant at $29 \pm 0.5^\circ\text{C}$. RH = relative humidity.

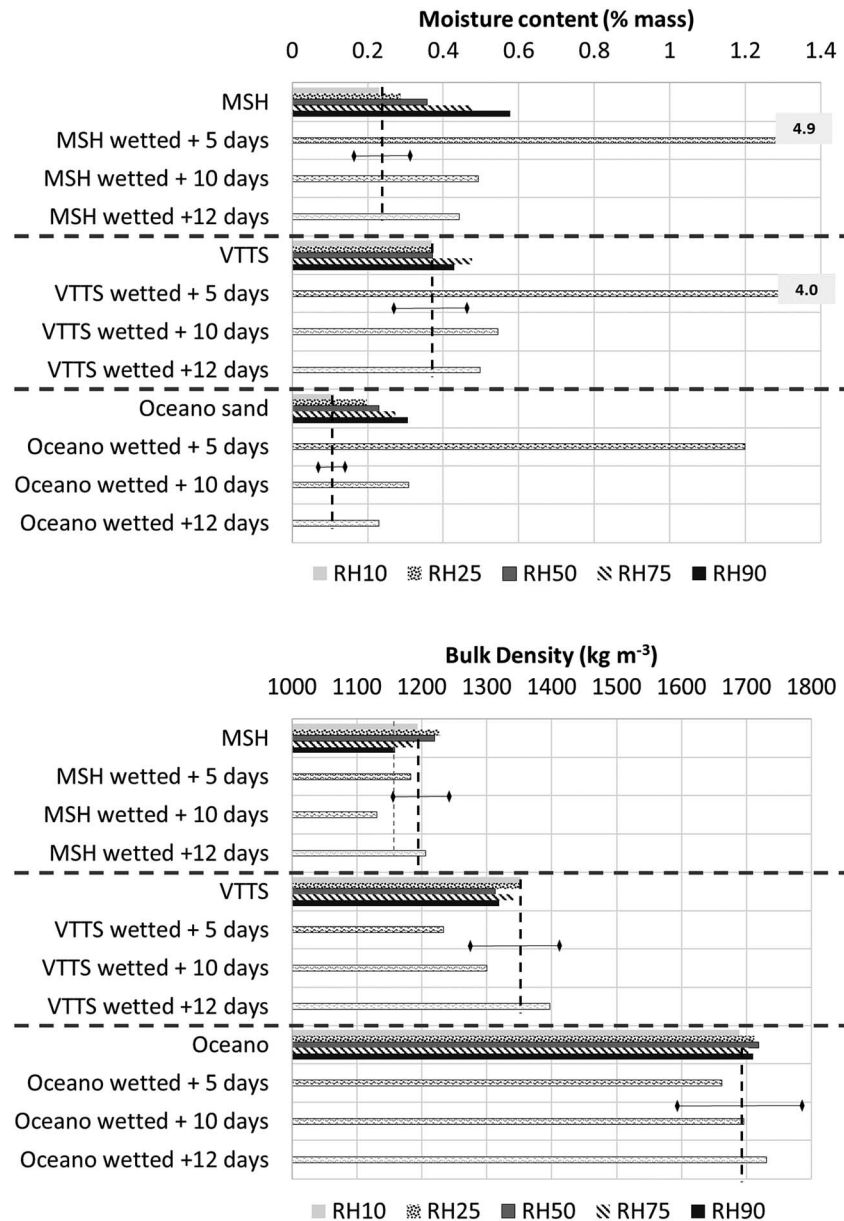


Figure 13. Summary of moisture content and bulk density. Vertical dashed lines indicate sample value during testing at RH = 50% prior to adding water. The horizontal lines show composite Std. dev.s obtained from averaging the standard deviations of replicate measurements for each of the source materials. (top) Moisture content. (bottom) Bulk density. MSH = Mount St. Helens; VTTS = Valley of Ten Thousand Smokes; RH = relative humidity.

across the surface with the sprayer nozzle. Once the application of water was completed, wax paper was placed on one of the quadrants of each sample box and overlain with a PVC plastic square (0.43 m × 0.43 m), onto which a masonry block that weighed 22.2 kg was placed. This provided a light, compressive pressure of 1,170 Pa. All sample boxes were conditioned at 29 °C and 50% RH for the duration of the third testing period. Testing was completed 5 days after water application (4 October 2017), 10 days after water application on the compressed surface (9 October 2017), and 12 days after water application (11 October 2017).

3.6. Bulk Density and Moisture Content

Samples of ash were collected to quantify bulk density (kg/m³) and moisture content (%) from each sample holder box at the end of PI-SWERL tests for that box. Samples were collected using a stainless steel

Table 1
Threshold Friction Velocities From First and Second Ramp Tests

RH or wetness condition	RH 15%	RH 25%	RH 50%	RH 75%	RH 90%	Rain + 5 days	Rain + 10 days	Rain + 12 days
Oceano sand								
<i>First ramp</i>								
Threshold u_* (m/s)	0.50	0.51	0.48	0.46	0.47	0.55	0.53	n/a
Std. dev. ^a	0.05	0.05	0.05	0.05	0.05	0.05	0.05	n/a
n	1	2	2	2	1	1	1	0
<i>Second ramp</i>								
Threshold u_* (m/s)	0.38	0.40	0.39	0.40	0.41	0.39	0.38	0.42
Std. dev. ^a	0.03	0.04	0.04	0.04	0.04	0.03	0.03	0.04
n	1	2	2	2	1	1	1	1
VTTS								
<i>First ramp</i>								
Threshold u_* (m/s)	0.24	0.27	0.27	0.30	0.31	0.35	0.44	0.38
Std. dev.	0.03	0.03	0.03	0.04	0.03	0.04	0.09	0.06
n	2	6	6	6	3	3	3	3
<i>Second ramp</i>								
Threshold u_* (m/s)	0.37	0.37	0.36	0.33	0.36	0.31	0.33	0.32
Std. dev.	0.03	0.03	0.04	0.03	0.08	0.03	0.03	0.03
n	2	6	6	6	3	3	3	3
MSH								
<i>First ramp</i>								
Threshold u_* (m/s)	0.26	0.29	0.31	0.35	0.35	0.35	0.30	0.34
Std. dev. ^a	0.03	0.03	0.04	0.03	0.03	0.03	0.04	0.03
n	4	8	8	7	4	4	4	1
<i>Second ramp</i>								
Threshold u_* (m/s)	0.37	0.37	0.39	0.40	0.43	0.43	0.41	0.44
Std. dev. ^a	0.03	0.03	0.05	0.04	0.06	0.04	0.04	0.04
n	4	8	8	8	4	4	4	4

Note. Two consecutive ramp tests were conducted on each test surface. The results from these two tests were sufficiently different to warrant separation.

^aWhere the number of replicate measurements was fewer than two, standard deviations were estimated as the average of standard deviations among samples where there were sufficient replicates to calculate standard deviations. RH = relative humidity; VTTS = Valley of Ten Thousand Smokes; MSH = Mount St. Helens; n/a = not applicable.

scoop (16.5 cm³ of volume per level scoop). The hemispherical scoop was lowered to the surface and rotated into the surface to cause minimal disturbance of the material and its packing. The scoop was slightly overfilled, but then carefully leveled to the full mark using a metal straight edge, again to minimize affecting the packing of the material. Using this technique, two scoops were collected from a portion of the test surface that was covered by the PI-SWERL during testing and were placed in a preweighed metal tin with a cover. Two additional scoops were collected from a portion of the test material that was not subjected to testing and were placed in a separate preweighed metal tin. The metal tins were weighed to a precision of 0.001 g (Denver Instrument, Bohemia, New York, Model APX-153) within 1 min of sample collection to ensure that the weight reflected the material prior to evaporation of any water. The metal tins were placed in the oven (149 °C) with loose covers and allowed to dry for 24 hr prior to being reweighed. Moisture content was taken as the mass of water in the sample divided by the mass of the sample. Bulk density was calculated as the mass of the collected material (including moisture) divided by the collected volume.

4. Results

4.1. Particle Characteristics

Using a scanning electron microscope, images of the MSH particles reveal abundant fresh, vesicular glass fragments (Figure 9) with angular, irregular shapes, and outer surfaces dominated by bubble outlines. Most surfaces appear fresh (lacking signs of clay alteration or weathering), with small adhering particles (Figure 9a-1), although a few surfaces are coated with precipitates (Figures 9a-2).

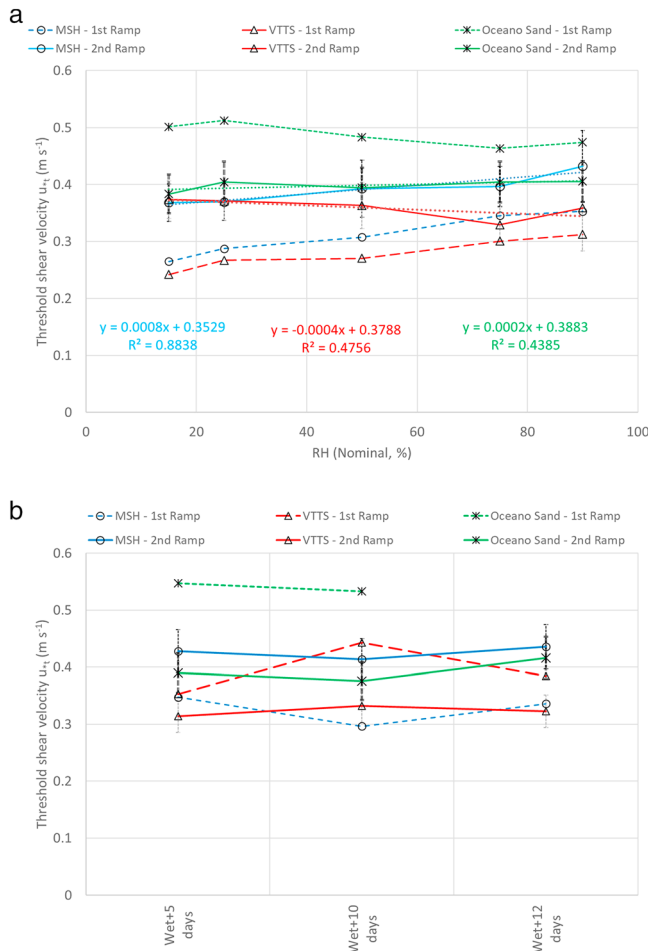


Figure 14. Threshold shear velocity, u_{*t} . Data are segregated by thresholds calculated from the first Ramp 3000 and second Ramp 3000 tests. Vertical bars represent standard deviations based on replicate measurements where available (shown only for second Ramp 3000 tests for clarity). (a) Threshold and RH. (b) Threshold after surface wetting and in 50% RH environment.

The ash collected from the VTTS is more variable than MSH ash and reflects both the different depositional environment and ageing since the eruption. Microscopically, the dominant fragments are angular particles of bubble-rich glass with adhering fines (Figure 10a) and crystals (Figure 10b). Many of the fragments have fuzzy surface coatings suggesting alteration or precipitates on their surfaces (Figure 10c).

4.2. Particle Size Distribution of VTTS and MSH Bulk and Resuspended Samples

Figure 11 shows the particle size distribution of bulk ash samples from VTTS and MSH, as well as the resuspended fraction collected from multiple PI-SWRL tests. The resuspended particles were collected from the hopper under conditions of u_{*} from 0.39 to 0.85 m/s during PI-SWRL testing. Keep in mind that the sample of resuspended ash underrepresents the real abundance of particles smaller than 2.5 μm and particles larger than about 20 μm due to the system design (section 3.5). This is illustrated in Figure 11 with a “cutoff” at 2.5 μm (vertical black line) and a shaded box from 5 μm (particles least impacted by cyclonic action) to 80 μm (all particles removed by cyclone). Despite the limitations of our sampling system, the observations are interesting—the resuspended material contains a surprising amount of particles >10 μm (17–25 vol% in these analyses). Notice the striking similarity in size distributions of resuspended ash from VTTS and MSH deposits in Figure 11, despite very different parent deposits. It is unclear if this similarity is partially an artifact of the sampling process or related to similarities in the size distribution of “resuspendable ash” in the parent deposits. Characterizing the size distribution of resuspendable ash from different types of deposits should be a topic for future experimental work. A final consideration in viewing the data from Figure 11 is that the resuspended ash was collected very near the deposit surface. It is unknown from these experiments how the size distribution would evolve in a lofted cloud over the minutes and hours following resuspension.

4.3. Ash Moisture and Bulk Density

The sample material (internal) RH essentially matched the set point targets in the environmental chamber (15%, 25%, 50%, 75%, and 90%) prior to testing (Figure 12). The change in moisture in the samples, expressed as the mean percent moisture content, is shown for MSH, VTTS, and Oceano Dune sand in Figure 13. Prior to the addition of liquid water, the moisture contents were extremely low for all three materials even under conditions of RH of 90%, with all values of moisture content <0.6%. Under the same RH conditions, Figure 13 shows that the bulk density was not sensitive to RH. The mean bulk densities and associated standard deviation of the mean for all RH conditions combined for the MSH, VTTS, and Ocean Dunes sand were, respectively, 1,338 kg/m³ (± 36 kg/m³), 1,505 kg/m³ (± 32 kg/m³), and 1,939 kg/m³ (± 68 kg/m³).

After the MSH 18 May eruption, the bulk density of the fall deposit was measured at varying distances from the volcano (Figure 339 of Sarna-Wojcicki et al., 1981). Before the first rainfall, it was very loosely packed, with bulk densities generally <1,000 kg/m³, and in some cases much lower. After the first rainfall, the bulk density increased at least twofold due to compaction. Based on this, bulk densities replicated in the laboratory studies presented here are a reasonable match to MSH ash fall deposits that have been exposed for a few days and subjected to rain.

4.4. Threshold Shear Velocity

Threshold shear velocity (u_{*t}) of each ash deposit was calculated from the data obtained during the Ramp 3000 tests (See Table 1). An example of the output of this type of test is shown in Figure 5. In the example shown, u_{*t} was visually determined to have occurred where the vertical dashed line crosses the x axis

Table 2
Summary of Emissions From Resuspension

RPM	1500		2000		2500		3000		3500	
u_* (m/s)	0.39		0.50		0.62		0.73		0.85	
	E_{PM10}	Std. dev.	E_{PM10}	Std. dev.	E_{PM10}	Std. dev.	E_{PM10}	Std. dev.	E_{PM10}	Std. dev.
Oceano sand										
RH 25%, $n = 2$	0.02	0.00	0.06	0.01	0.15	0.01	0.40	0.04	0.99	0.06
RH 50%, $n = 2$	0.04	0.01	0.10	0.02	0.26	0.05	0.62	0.04	1.8	0.1
RH 75%, $n = 2$	0.04	0.00	0.06	0.01	0.12	0.02	0.37	0.05	0.85	0.03
Rain + 5 days, $n = 2$	0.04	0.00	0.08	0.02	0.17	0.01	0.57	0.00	1.4	0.2
Rain + 10 days, $n = 2$	0.10	0.03	0.12	0.03	0.26	0.03	0.69	0.15	1.4	0.2
Rain + 12 days, $n = 2$	0.08	0.02	0.10	0.01	0.21	0.04	0.38	0.05	0.69	0.18
VTTS										
RH 25%, $n = 6$	1.7	0.5	9.1	2.4	18	4	34	8	70	18
RH 50%, $n = 6$	2.7	1.2	9.6	2.8	20	5	42	10	82	18
RH 75%, $n = 6$	1.1	0.4	3.1	0.8	6.6	1.5	13	3	26	5.8
Rain + 5 days, $n = 6$	0.97	0.28	2.9	0.6	6.1	0.8	13	1	30	3
Rain + 10 days, $n = 5$	0.72	0.38	2.4	1.0	5.1	1.9	11	4	25	8
Rain + 12 days, $n = 6$	1.9	0.7	4.7	1.5	9.7	2.4	20	5	43	10
MSH										
RH 25%, $n = 8$	11	4	67	10	180	10	350	10	530	10
RH 50%, $n = 8$	6.0	2.4	36	11	110	20	280	30	430	40
RH 75%, $n = 8$	3.6	1.2	17	4	60	8	130	10	250	20
Rain + 5 days, $n = 7$	5.4	2.8	26	9	98	21	230	20	360	30
Rain + 10 days, $n = 8$	4.4	1.8	20	7	69	16	170	20	280	20
Rain + 12 days, $n = 8$	6.9	3.7	22	9	70	20	150	30	230	30

Note. RPM = revolution per minute; RH = relative humidity; VTTS = Valley of Ten Thousand Smokes; MSH = Mount St. Helens.

230 s into the test. At this point in the test, the annular blade was rotating at 1,411 RPM. Although this visual identification is somewhat subjective, when viewed on a logarithmic scale, it is generally easy to identify the point at which the PM_{10} concentrations measured by the DustTrak begin to rise consistently with the increasing rate of blade rotation. The threshold RPM is converted into a u_{*t} value using the relationship from Etyemezian et al. (2014)

$$u_* = C_1 \alpha^4 RPM^{C_2/\alpha} \quad (7)$$

where C_1 is a constant (=0.000683), C_2 is a constant (=0.832), and α has the assigned value of 0.90 for all surfaces tested (based on the surface roughness designation), giving an equivalent u_{*t} of 0.37 m/s in the example shown in Figure 5.

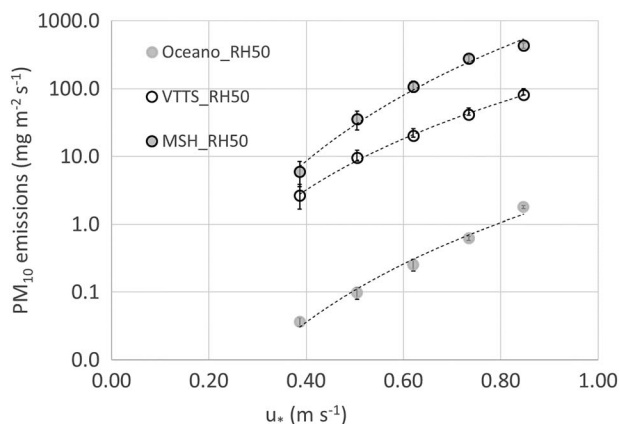


Figure 15. PM_{10} resuspension emissions at RH of 50% for the three samples tested. The dashed lines are power law regression fits (equations omitted for clarity). Vertical bars are standard errors and represent the precision of the measurement. RH = relative humidity; VTTS = Valley of Ten Thousand Smokes; MSH = Mount St. Helens; PM = particulate matter.

The first of the two successive Ramp 3000 tests in nearly all cases provided a lower u_{*t} estimate than the second for MSH and VTTS samples. We attribute this to the test surface being initially overly prone to particle entrainment because of the mixing and smoothing during preparation. Following the first test, the most readily suspendable material would be removed and unavailable for the second test. In contrast, for Oceano Dune sand, the first Ramp 3000 test consistently gave a higher u_{*t} than the second test. A possible explanation is that the flattening of the sand surface during sample preparation increased the threshold. However, once sediment transport initiates, the surface rapidly assumes an uneven form with ripples and other regular features. These features apparently reduce the threshold for transport on sandy surfaces. In all cases, we propose that the threshold measured during the second Ramp 3000 test is more meaningful as it more closely represents a surface that has been exposed to environmental conditions.

For the u_{*t} values (from second Ramp 3000 tests) shown in Figure 14a, the ranges of u_{*t} over the RH range of 15% to 90% are 0.37 m/s (± 0.03 m/s) to 0.43 m/s (± 0.06 m/s) for the MSH samples, 0.33 m/s (± 0.03 m/s) to 0.37

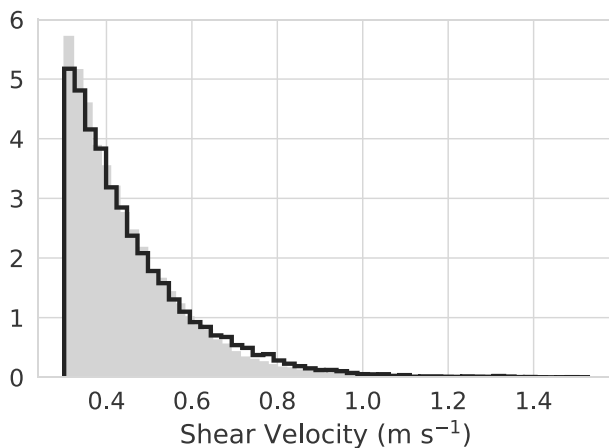


Figure 16. Distribution of u_* values when $u_* > 0.30$ m/s from weather research and forecasting model output for 1980–2010 for Hanford, Washington. Solid gray is for areas of shrub land, and the black line is for areas of dry crop land.

m/s (± 0.07 m/s) for the VTTS samples, and 0.38 m/s (± 0.03 m/s) to 0.41 m/s (± 0.04 m/s) for the Oceano Dunes sand. Linear regression shows that with increasing humidity, u_{*t} increases slightly for MSH and Oceano sand but decreases slightly for the VTTS sample. However, we suggest that the relationship between humidity and threshold shear relationship is modest at best, due to the high standard deviations and the subjective identification of u_{*t} from PI-SWERL tests (see section 3.5).

Figure 14b shows the u_{*t} values measured 5, 10, and 12 days after wetting the sample with the equivalent of 5 mm of rain. Note that the deposit 10 days after wetting also experienced compaction from the masonry block over the 10-day period. These measurements were not found to differ systematically from the wetted-only surfaces, and any additional compaction offered by the block is hereafter assumed to have had a negligible effect.

From these tests simulating the effects of light rainfall, we again saw a notable difference between u_{*t} from the first and second Ramp 3000 tests. For MSH, u_{*t} is higher for the second test (consistent with the experiments varying humidity), indicating that the surface initially releases some readily suspended particles. In contrast, the VTTS samples have a higher u_{*t} for

the first test. The application of liquid water may result in the formation of a protective crust, perhaps due to the more altered state of the VTTS ash with more abundant clay and/or precipitates (refer to SEM images and particle description). Once destroyed by the first test, the crust no longer provides protection.

An overall finding is that the differences in u_{*t} from simulated rainfall are essentially the same as those observed from varying the RH. Therefore, if there is an effect of wetting (such as by formation of a thin crust in the VTTS sample), it is not one that endures under active wind erosion conditions. Moreover, the RH sensors embedded in the test boxes were measuring RH in excess of 95% up to 10 days after wetting. The RH in the environmental chamber was set at 50% and prior experience indicated that the RH within the test boxes would equilibrate with chamber RH within 10 hr or so. The near 100% RH 10 days after wetting indicates the continued presence of liquid water in the sample boxes. Even during the testing conducted 12 days after wetting, the RH in only four of the test boxes had dropped below 95% (ranging from 70% to 85%), indicating the presence of at least some amount of liquid water in the sample box. This suggests that the proximity of liquid water (at least 3 cm below the surface) to the surfaces tested did not have an impact on u_{*t} .

4.5. Particle Emission Rates

The PM₁₀ emission rates for ash by resuspension as a function of u_* are summarized in Table 2. They are compared among the VTTS, MSH, and Oceano samples at an RH of 50% in Figure 15. For comparable u_* values, resuspension emissions from VTTS ash are almost 2 orders of magnitude greater than from Oceano Dune sand. MSH ash emissions are another half an order of magnitude higher. In all cases, the differences are greater than measurement uncertainty, expressed as standard errors (standard deviation divided by the square root of the number of samples less one).

It is helpful to compare the range of u_* that was simulated in the laboratory setting with the actual setting of the ash deposits. Direct measurements of u_* are not routinely reported from surface meteorological monitoring networks, but numerical weather prediction models such as the weather research and forecasting (WRF) model do provide forecasts of wind speeds as well as u_* . The output of the WRF model for Hanford as described in Ngan and Stein (2017) from 1980 to 2010 was available for this type of analysis. Between 1980 and 2010, wind speeds estimated by the WRF model (with 27-km resolution) at about 8 m AGL ranged from 0 to about 18 m/s. The link between wind speed and u_* (see equation (5)) is provided by an assumed gross aerodynamic roughness height (z_0). In WRF, the area around Hanford is classified mostly as shrub land ($z_0 = 0.01$ – 0.05 m), dry crops ($z_0 = 0.05$ – 0.15 m), and irrigated crops ($z_0 = 0.02$ – 0.1 m) with some grassland ($z_0 = 0.1$ to 0.12 m). Shear velocities as high as 1.4 m/s were computed over the same period, although the majority were under 0.6 m/s (Figure 16). Shrub land, which has lower aerodynamic roughness lengths, had, on average, higher wind speeds but lower u_* values.

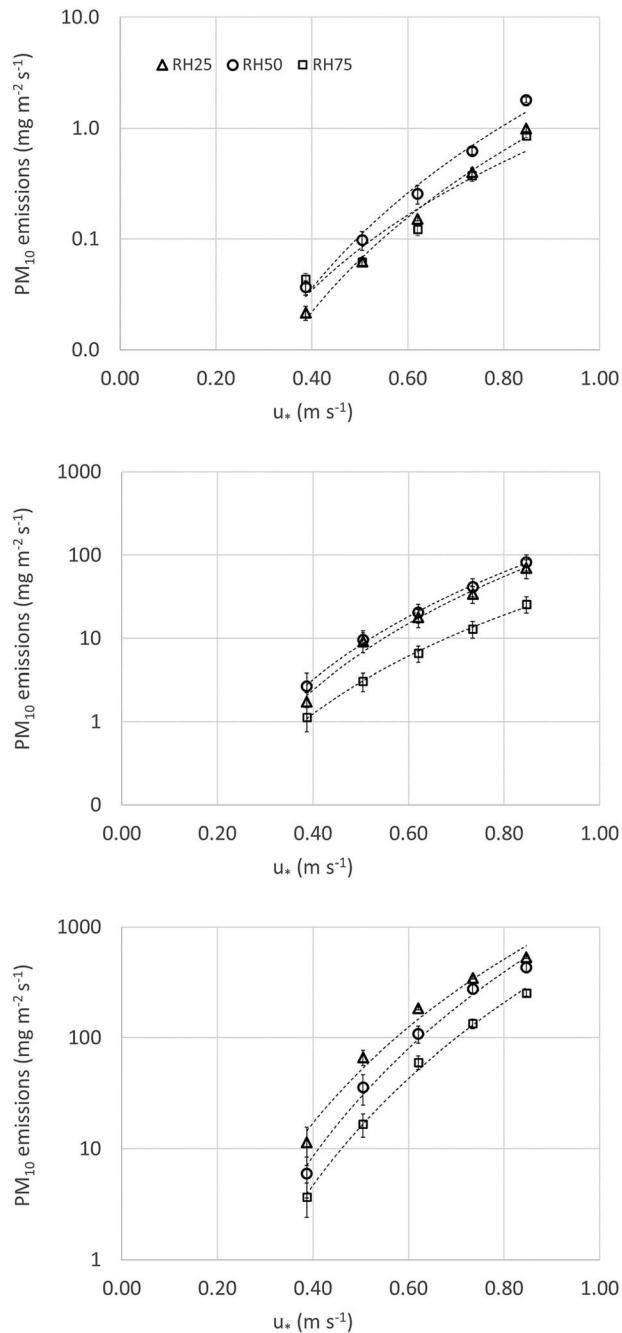


Figure 17. PM_{10} resuspension emission with varying shear velocity and RH. Vertical bars are standard error of the mean emission rate based on replicate sampling. (top) Oceanic sand, (middle) Valley of Ten Thousand Smokes ash, and (bottom) Mount St. Helens ash. RH = relative humidity; PM = particulate matter.

It is important to note that the shear stress that is imparted onto the gross landscape is not equal to the shear stress (same for u_*) that is experienced by the deposited ash that is in between surface physical roughness elements such as shrubs, where it is reasonable to expect that the overwhelming majority of deposited ash will be. Given that the relationships developed in the present work are for a bare surface, it is appropriate to consider a shear stress partitioning scheme (e.g., Gillies et al., 2007; Raupach et al., 1993; Shao & Yang, 2008), whereby the shear velocity provided by an NWP model for the gross landscape is adjusted to account for the protection that is offered from roughness elements. Pierre et al. (2014) and King et al. (2005) provide useful comparisons of drag partition schemes. The Marticorena and Bergametti (1995) relationship adapted by MacKinnon et al. (2004) is useful as it only requires knowledge of the aerodynamic roughness length, which can be supplied by the NWP model. Assuming an aerodynamic roughness of 0.001 m for a bare ash surface, the Marticorena and Bergametti (1995) relationship used in Pierre et al. (2014) gives a shear stress adjustment factor of 0.74 for gross landscape roughness of $z_0 = 0.01$ m (shrub land) and 0.44 for $z_0 = 0.15$ m (dry crops). Noting that u_* is proportional to the square root of the shear stress and that the highest value of u_* achieved during in-lab testing (corresponding to 3500 RPM) was 0.85 m/s, then it can be estimated that the measurements reported here are directly applicable to gross landscape u_* values up to 1.0 m/s for shrub land and 1.3 m/s for dry cropland. These are comparable to the top end of the values shown in Figure 16, indicating that the measurements conducted in the lab occurred over a range of u_* values that is relevant for in situ conditions.

Numerical weather model predictions of u_* were not as readily available for VTTS. Similar shear stress partitioning considerations would apply as for the Hanford location when translating u_* provided at some height above the surface at VTTS (e.g., by a numerical model or meteorological tower) into the shear that is experienced by the wind-erodible portion of the ash, the portion that was subjected to testing in the laboratory measurements described here.

Changes in emission rates due to changes in ambient humidity are shown in Figure 17. Overall, the effect of humidity is modest compared to differences between samples. The Oceano Dune sand does not show a clear trend, perhaps related to a smaller number of samples (one sample box compared to three from VTTS and four from MSH). We note that the magnitude of emissions is in line with what Etyemezian and Gillies (2016) reported for in situ measurements conducted in the field at the Oceano Dunes (median values of 0.05, 0.6, and 1.4 $mg \cdot m^{-2} \cdot s^{-1}$ at equivalent u_* of 0.50, 0.73, and 0.85 m/s, respectively—when a value of $\alpha = 0.90$ is used for conversion between PI-SWERL RPM and u_* , as was done in the present work).

The VTTS and MSH samples both show a decrease in emissions at the highest RH of 75% (Figure 17). These effects are significant even considering the variability of the measurements, which are expressed as the standard error of sampling in Figure 17.

Consistent with prior work (e.g., Ishizuka et al., 2014), the general relationship between particulate matter emissions and u_* , for the ash and sand materials, appears to be well represented by a power law equation of the type (see also equation (4))

Table 3
Fitting Parameters to Equation (9)

Source material	RH condition	Emission function parameters		Emission function parameter uncertainties for log-transformed parameters	
		a	b	a	b
VTTS	25%	4.53	2.18	0.32	0.08
	50%	4.30	2.21	0.11	0.03
	75%	3.94	1.66	0.11	0.03
Rain plus 5 days	50%	4.26	1.72	0.21	0.05
Rain plus 10 days + light compression	50%	4.41	1.67	0.18	0.05
Rain plus 12 days	50%	3.94	1.86	0.20	0.05
MSH	25%	4.91	3.18	0.43	0.11
	50%	5.53	3.13	0.34	0.09
	75%	5.48	2.85	0.19	0.05
Rain plus 5 days	50%	5.51	3.05	0.31	0.08
Rain plus 10 days + light compression	50%	5.40	2.90	0.23	0.06
Rain plus 12 days	50%	4.63	2.75	0.20	0.05
Oceano	25%	4.83	0.27	0.29	0.07
	50%	4.89	0.50	0.37	0.09
	75%	3.85	0.07	0.66	0.17
Rain plus 5 days	50%	4.68	0.36	0.55	0.14
Rain plus 10 days + light compression	50%	3.55	0.30	0.61	0.15
Rain plus 12 days	50%	2.90	-0.02	0.39	0.10

Note. RH = relative humidity; VTTS = Valley of Ten Thousand Smokes; MSH = Mount St. Helens.

$$EF10 = cu_*^a \quad (8)$$

where the coefficients c and a are obtained by fitting the PI-SWERL data as shown in Figure 17. This fit is more straightforward to conceive of as a linear fit to the log transform of equation (8)

$$\text{Log}_{10} (EF10 [PM_{10} \text{ mg m}^{-2}\text{s}^{-1}]) = a\text{Log}_{10}(u_* [\text{m/s}]) + b \quad (9)$$

A summary of the parameters a and b for the data collected during this study is provided in Table 3.

Figure 18 shows the effect of simulated rain followed by drying at RH of 50% for 5, 10, and 12 days of elapsed time from sample wetting. Results are compared with emission factors measured without the addition of water (also at 50% humidity). The VTTS samples appear to be affected by the addition of water, with emission factors lowered by a factor of approximately 3 for 5 and 10 days following the application of simulated rain (10 days following application is when testing on the slightly compressed quadrant was completed). By the twelfth day after water application, emission factors remained statistically below but were returning to prewetted values. The effect is more subtle for the MSH samples. Generally, the wetted surfaces had slightly lower emissions than the unwetted surface, but there does not seem to be a relationship between the time that the surface was allowed to dry and the emission factors (e.g., emission factors 12 days after water application appear to be slightly lower than 5 days after water application, which is not what is expected). In any case, differences in emissions were comparable to the standard errors of the measurements and it is unclear if such differences could be considered statistically significant. The sample from the Oceano Dunes does not exhibit a consistent relationship between days after application of water and magnitude of emission factors. Again, this may be because of the comparatively small sample size.

5. Discussion

5.1. Threshold Shear Velocity

The estimated mean values for u_{*t} (and the associated standard deviations) for the MSH, VTTS, and Oceano Dune sand samples over the range of RH conditions tested are, 0.39 m/s (± 0.03 m/s), 0.40 m/s (± 0.01 m/s), and 0.36 m/s (± 0.02 m/s), respectively. The data shown in Figure 14 suggest that the effect of RH on u_{*t} for

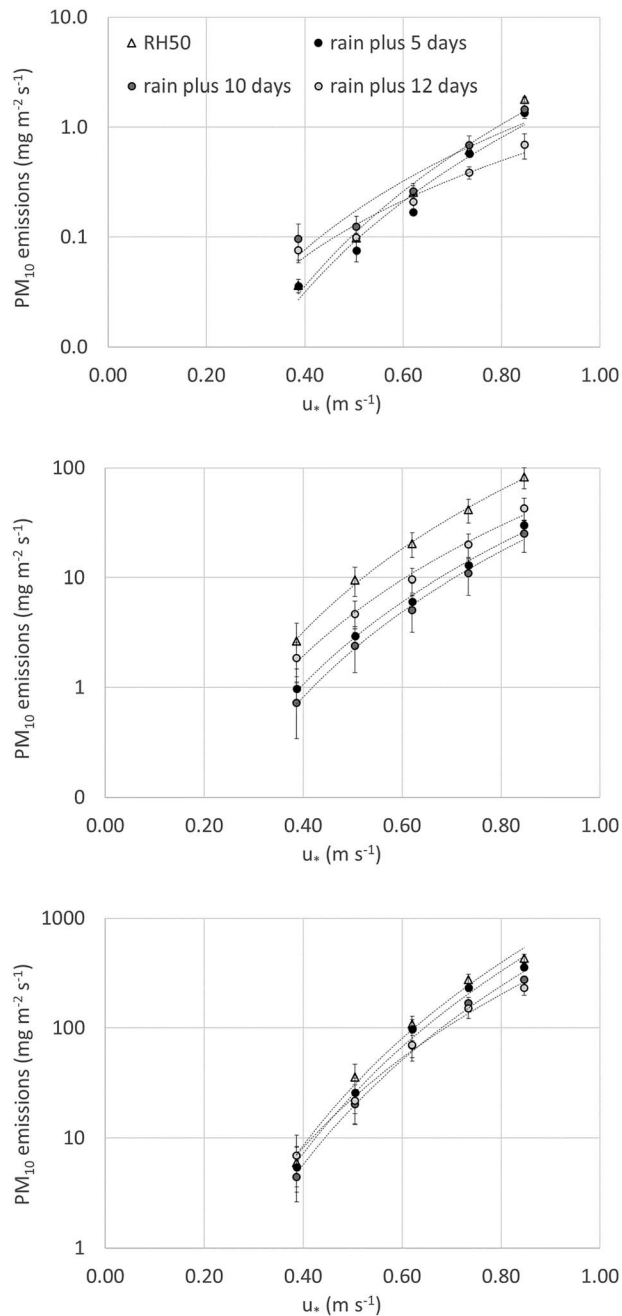


Figure 18. PM₁₀ resuspension emissions 5, 10, and 12 days after the addition of water equivalent to 5 mm of rainfall. Vertical bars are standard error of the mean emission rate based on replicate sampling. (top) Oceanosand, (middle) Valley of Ten Thousand Smokes ash, and (bottom) Mount St. Helens ash. RH = relative humidity; PM = particulate matter.

these ash samples is limited. In the case of the MSH samples from the present work, increasing the RH from 15% to 50% increased u_{*t} by 7%. However, crust formation did not appear to be a relevant process based on the observation that surface emissions were unchanged after simulated rainfall (Figure 18). For comparison, Ravi and D’Odorico (2005) reported for mineral soils in California’s Mojave Desert and the Canyonlands region in Utah a relative increase in threshold wind speed measured at 3 m AGL (resulting in the same relative increase in u_{*t} ; see equation (5)), between 12% (Crucero, CA site) and 24% (Soda Lake, CA site) for the change from <10% RH to $\approx 35\%$. Del Bello et al. (2018) reported an increase in u_{*t} by $\approx 50\%$ for sieved particles (<63 μm) from ash from the Campi Flegrei region of Italy and $\approx 130\%$ for the same size range for ash from the 2010 Eyjafjallajökull eruption in Iceland. Little or no change in u_{*t} was observed for larger particle size fractions (63–125 and 125–250 μm) from those two sources as a result of varying the RH between 10% and 90%.

VTTS samples showed a more ambiguous relationship to humidity. Increasing the RH from 50% to 75% lowered the threshold for the deposit slightly (c.f., Ravi & D’Odorico, 2005), but the difference was of comparable magnitude to the uncertainty of the measurements.

For other locations where u_{*t} for volcanic ash deposits has been estimated from available wind data, or modeled, the range of reported values is quite restricted. Folch et al. (2014), Leadbetter et al. (2012), and Liu et al. (2014) report values of 0.4 m/s for u_{*t} for deposits in Argentina and Iceland. Thorsteinsson et al. (2011) report a u_{*t} of 0.42 m/s for ash deposits in Iceland, matching closely the model-derived value of Liu et al. (2014). These values are consistent with our results (0.39 and 0.40 m/s for MSH and VTTS, respectively). Compared to threshold wind speeds suggested by Fowler and Lopushinsky (1986) of (2.5–3 m/s), our results support higher threshold wind speeds that are close to 8 m/s at 10 m AGL, assuming a surface aerodynamic roughness of 0.005 m, which corresponds to a relatively smooth, non-vegetated surface. Although Sehmel (1982) also supported the lower threshold wind speeds for MSH that were estimated by Fowler and Lopushinsky (1986), it was also suggested that their field measurements could have been biased by emissions from an area upwind.

5.2. Particle Emission Rates

Resuspension of volcanic ash by wind has been recognized to be a potentially significant source of regional atmospheric particle loading (Hadley et al., 2004; Leadbetter et al., 2012, among others), and this is strongly supported by our experimental measurements. Ash deposits from VTTS and MSH are among the highest emitting sources ever measured.

Our resuspension relationships for the VTTS and MSH samples (Figure 17) are compared to the range of emissions for mineral dusts made during various field studies in Figure 19. The lower gray-shaded area bounds the range of emissions reported from six field studies (Gillette, 1979; Gomes et al., 2003; Nickling & Gillies, 1993; Nickling et al., 1999; Sow et al., 2009) as compiled by Kok et al. (2012). The upper shaded area bounds the range of emissions reported for the Slims River delta sediments in the Yukon Territory of Canada, by Nickling (1978). Emission rates from these deltaic sediments (Nickling, 1978), which were composed of $\approx 53\%$ medium to very fine sand (500- to 62.5- μm diameter), $\approx 45\%$ silt (4–62 μm), and 2% clay ($\leq 2 \mu\text{m}$), are, to our knowledge, among the highest reported in the literature

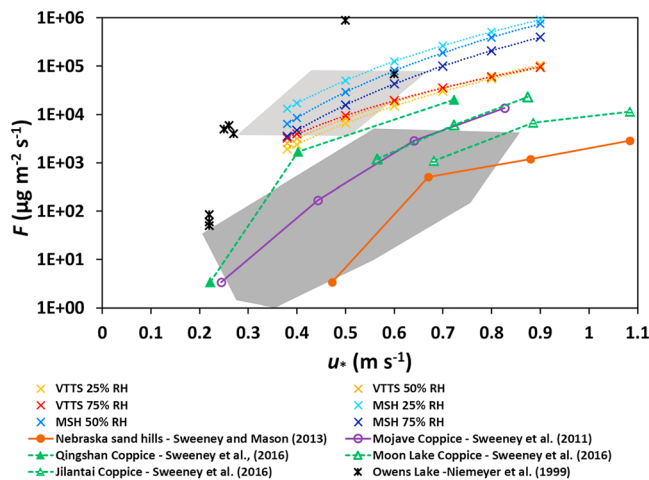


Figure 19. Emissions of dust measured using the PI-SWRL for the VTTS and MSH samples compared with available field data reported for surfaces emitting mineral dust. The VTTS and MSH emissions are represented by the best fit lines from Figure 17. The lower gray polygon bounds emissions measurements reported in six studies from various locations around the globe (as summarized by Kok et al., 2012). The upper gray polygon bounds the emission data of Nickling (1978) as reported by Kok et al. (2012). The hatched lines with triangle symbols represent emissions measured using PI-SWRL by Sweeney et al. (2016) for coppice dune areas in China. The solid lines with circle symbols represent emissions measured using PI-SWRL in the Nebraska Sand Hills (brown, solid circles) by Sweeney and Mason (2013) and in Mojave Desert coppice dune areas (purple, open circles) by Sweeney et al. (2011). The symbols represent data from Owens Lake as determined from sun photometry data by Niemeier et al. (1999). VTTS = Valley of Ten Thousand Smokes; MSH = Mount St. Helens.

and/or measurements from analog experiments (e.g., present study; Fowler & Lopushinsky, 1986; Bristow & Moller, 2018).

6. Conclusions

This study characterizes volcanic ash resuspension from two of the twentieth Century's most significant volcanic eruptions in North America—MSH 1980 and Katmai 1912 in the VTTS, Alaska. Laboratory tests conducted with a portable wind tunnel and environmentally conditioned samples of ash from these eruption deposits indicate a threshold shear velocity for ash mobilization that is not very sensitive to RH and with a value of ≈ 0.4 m/s, which is in line with previous studies from field measurements and modeling.

The relationships between particle emission rates and shear velocity indicate that the MSH and VTTS ashes are some of the most erodible deposits yet quantified. Over the u_* range of 0.4 to 1 m/s, the emission of PM_{10} ranges from 10 to $>100 \text{ mg} \cdot \text{m}^{-2} \cdot \text{s}^{-1}$. These emission rates have the potential to adversely impact human, animal, and possibly plant health due to extremely high mass concentration levels of airborne particulate matter under elevated wind shear conditions. The resultant concentrations of airborne ash may also reach levels that threaten the capacity of air handling systems in industrial facilities. The actual severity will be dependent upon the duration of the elevated shear stress conditions.

Among the deposits tested, at constant RH (50%), MSH resuspension emissions at comparable shear velocities were a factor of 3 or so higher than VTTS, which were in turn 2 orders of magnitude higher than PM_{10} emissions from a control dune sand sample. At higher RH (75%) resuspension emissions of VTTS and MSH were attenuated (by a factor of 3 or so) compared to lower RH levels (25%, 50%). Wetting of the samples to the equivalent of 5 mm of rainfall followed by subsequent drying at RH of 50% showed that MSH was virtually unaffected by liquid water once the surface was dry (<5 days). Wetting of VTTS appeared to attenuate resuspension emissions for a longer duration (at least 12 days).

for wind erosion. These latter rates reported by Nickling (1978) appear to envelope the VTTS ($\approx 74\%$ sand, $\approx 24\%$ silt, $\approx 1\%$ clay) and MSH ($\approx 29\%$ sand, $\approx 71\%$ silt, $<1\%$ clay) emissions data. Note that the MSH and VTTS emissions are reported for PM_{10} and those measured by Nickling (1978) likely included larger particles. The emission rates of VTTS and MSH would increase if the measured airborne particle size range was modified to include the particles $>10 \mu\text{m}$ in aerodynamic diameter. We estimate that the emission rates could be 20% higher based on the size distribution of resuspended ash in Figure 11 but even this is probably an underestimate because the PI-SWRL imposes its own particle size cutoff on larger particles.

The measurements made in this study show that fresh ash deposits (simulated by reconditioned VTTS and MSH samples at bulk densities of $1,200\text{--}1,350 \text{ kg/m}^3$) are extremely emissive and highly susceptible to resuspension. The potential emissions from resuspension of ash deposits similar to VTTS and MSH samples would represent a significant risk to human health for people in the vicinity of such emissions. An important caveat to this is that the emissions reported are for relatively smooth, non-vegetated surfaces. The presence of vegetation and other nonerodible roughness within the terrain could significantly reduce resuspension. Increasing amounts of nonerodible roughness elements will require higher regional wind speeds to reach the threshold shear velocity (Gillies et al., 2007; Raupach et al., 1993; Shao & Yang, 2008).

Direct measurements of emissions are needed to validate estimates derived from physical models of resuspension potential (e.g., Folch et al., 2014), inferred emissions and thresholds based on ambient concentrations of ash particles (e.g., Lui et al., 2014; Thorsteinsson et al., 2012),

Author Contribution

V. Etyemezian, J. Gillies, R. Hasson, and G. Nikolich designed the experiments; V. Etyemezian carried them out with assistance from J. Gillies and G. Nikolich. L. Mastin, and A. Van Eaton provided analyses of bulk ash and resuspended samples. V. Etyemezian, J. Gillies, and A. Crawford developed the empirical models for ash particle emission. V. Etyemezian prepared the manuscript with contributions from all coauthors.

Acknowledgments

This work was funded by the Department of Energy (DOE), Office of River Protection (ORP) under contract number DE-EM0003968. The authors also thank the NPS and Katmai National Park and Preserve for granting access and collection of ash samples from the Valley of Ten Thousand Smokes under permit: KATM-2016-SCI-0009 for study: KATM-00132. We also gratefully acknowledge Peter Frenzen, Mount St. Helens National Volcanic Monument, and the helicopter support from JL Aviation, Boring, Oregon, for the MSH ash collection and Egli Air Haul, Inc., King Salmon, Alaska, for the ash collection in the VTTS. The authors wish to thank Judith Fierstein (USGS) for information prior to and following VTTS sampling as well as Hans F. Schwaiger (USGS) for helpful comments on the manuscript. Any views, opinions, or endorsements expressed in the text belong solely to the authors and do not reflect explicit or implied support or consent from the DOE ORP and U.S. National Park Service (NPS). Sample collection methods and experimental procedures were developed and executed in accordance with EM-QA-001, EM Quality Assurance Program (QAP; US DOE, 2012) and ASME NQA-1-2008/2009a, *Quality Assurance Requirements for Nuclear Facility Applications* (ASME, 2013). The guidance on control of scientific investigations in NQA-1a-2009, Part III Subpart 3.2 (ASME, 2013) was utilized to perform this research. Data used for this manuscript are under the curation of the U.S. Department of Energy, Office of River Protection. Requests for data should be directed to the U.S. Department of Energy, Environmental Management Consolidated Business Center, Cincinnati, OH 45202, USA. Any use of trade, firm, or product names is for descriptive purposes only and does not imply endorsement by the U.S. Government.

References

- Alexander, A. E. (1934). The dustfall of November 13, 1933 at Buffalo, New York. *Journal of Sedimentary Petrology*, 4(2), 81–82. <https://doi.org/10.2110/jsr.4.81>
- Arnalds, O., Thorarinsdottir, E. F., Thorsson, J., Waldhauserova, P. D., & Agustsdottir, M. (2013). An extreme wind erosion event of the fresh Eyjafjallajökull 2010 volcanic ash. *Scientific Reports*, 3, 1257. <https://doi.org/10.1038/srep01257>
- ASME (2013). ASME-NQA-1-2012: Quality Assurance requirements for nuclear facility applications, American Society of Mechanical Engineers, Two Park Avenue, New York, New York, USA. March 15, 2013.
- Bacon, C. R., & Lanphere, M. A. (2006). Eruptive history and geochronology of Mount Mazama and the Crater Lake region, Oregon. *Geological Society of America Bulletin*, 118(11-12), 1331–1359. <https://doi.org/10.1130/B25906.1>
- Bagnold, R. A. (1941). *The physics of blown sand and desert dunes*, (p. 265). London: Chapman and Hall.
- Ball, J. G. C., Reed, B. E., Grainger, R. G., Peters, D. M., Mather, T. A., & Pyle, D. M. (2015). Measurements of the complex refractive index of volcanic ash at 450, 546.7, and 650 nm. *Journal of Geophysical Research: Atmospheres*, 120, 7747–7757. <https://doi.org/10.1002/2015jd023521>
- Barsotti, S., Andronico, D., Neri, A., Del Carlo, P., Baxter, P. J., Aspinall, W. P., & Hincks, T. (2010). Quantitative assessment of volcanic ash hazards for health and infrastructure at Mt. Etna (Italy) by numerical simulation. *Journal of Volcanology and Geothermal Research*, 192(1-2), 85–96. <https://doi.org/10.1016/j.jvolgeores.2010.02.011>
- Baxter, P. J. (1999). Impacts of eruptions on human health. In H. Siggurdson (Ed.), *Encyclopaedia of Volcanoes*, (pp. 1035–1043). New York: Academic Press.
- Beckett, F., Kylling, A., Sigurðardóttir, G., von Löwis, S., & Witham, C. (2017). Quantifying the mass loading of particles in an ash cloud remobilized from tephra deposits on Iceland. *Atmospheric Chemistry and Physics*, 17, 4401–4418. <https://doi.org/10.5194/acp-17-4401-2017>
- Belly, P. Y. (1964). *Sand movement by wind*. Washington, DC: U.S. Army Corps of Engineers, Coastal Engineering Research Center.
- Belnap, J., & Gillette, D. A. (1997). Disturbance of biological soil crusts: Impacts on potential wind erodibility of sandy desert soils in southeastern Utah. *Land Degradation and Development*, 8(4), 355–362. [https://doi.org/10.1002/\(SICI\)1099-145X\(199712\)8:4<355::AID-LDR266>3.0.CO;2-H](https://doi.org/10.1002/(SICI)1099-145X(199712)8:4<355::AID-LDR266>3.0.CO;2-H)
- Bernstein, R. S., Baxter, P. J., Falk, H., Ing, R., Foster, L., & Frost, F. (1986). Immediate public health concerns and actions in volcanic eruptions: Lessons from the Mount St. Helens eruptions, May 18–October 18, 1980. *American Journal of Public Health*, 76(Suppl), 25–37. <https://doi.org/10.2105/AJPH.76.Suppl.25>
- Bonadonna, C., Mayberry, G. C., Calder, E. S., Sparks, R. S. J., Choux, C., Jackson, A. M., et al. (2002). Tephra fallout in the eruption of Soufrière Hills Volcano, Montserrat. In T. H. Druitt, & B. P. Kokelaar (Eds.), *The eruption of Soufrière Hills Volcano, Montserrat, from 1995 to 1999*, (pp. 483–516). London: Geological Society of London.
- Bristow, S. W., & Moller, T. H. (2018). Dust production by abrasion of aeolian basalt sands: Analogue for Martian dust. *Journal of Geophysical Research: Planets*, 123(10), 2713–2731. <https://doi.org/10.1029/2018JE005682>
- Castro, J., & Dingwell, D. B. (2009). Rapid ascent of rhyolitic magma at Chaitén volcano, Chile. *Nature*, 461(7265), 780–783. <https://doi.org/10.1038/nature08458>
- Criswell, W. (1987). Chronology and pyroclastic stratigraphy of the May 18, 1980 eruption of Mount St. Helens, Washington. *Journal of Geophysical Research*, 92(B10), 10,237–10,266. <https://doi.org/10.1029/JB092iB10p10237>
- Dagsson-Waldhauserova, P., Arnalds, O., & Olafsson, H. (2013). Long-term frequency and characteristics of dust storm events in Northeast Iceland (1949–2011). *Atmospheric Environment*, 77, 117–127. <https://doi.org/10.1016/j.atmosenv.2013.04.075>
- Dartevelle, S., Ernst, G., Stix, G. J., & Bernard, A. (2002). Origin of the Mount Pinatubo climactic eruption cloud: Implications for volcanic hazards and atmospheric impacts. *Geology*, 30(7), 663–666. [https://doi.org/10.1130/0091-7613\(2002\)030<0663:OOTMPC>2.0.CO;2](https://doi.org/10.1130/0091-7613(2002)030<0663:OOTMPC>2.0.CO;2)
- Del Bello, E., Taddeucci, J., Merrison, J. P., Alois, S., Iversen, J. J., & Scarlato, P. (2018). Experimental simulations of volcanic ash resuspension by wind under the effects of atmospheric humidity. *Scientific Reports*, 8, 14509. <https://doi.org/10.1038/s41598-018-32807-2>
- Durant, A. J., Rose, W. I., Sarna-Wojcicki, A. M., Carey, S., & Volentik, A. C. M. (2009). Hydrometeor-enhanced tephra sedimentation: Constraints from the 18 May 1980 eruption of Mount St. Helens. *Journal of Geophysical Research*, 114, B03204. <https://doi.org/10.1029/2008JB005756>
- Etyemezian, V., & Gillies, J. A. (2016). Updated wind erodibility measurements at and near the Oceano Dunes State Vehicular Recreation Area. Prepared for California Department of Parks and Recreation, Oceano Dunes District. March 30, 2016.
- Etyemezian, V., Gillies, J. A., Shinoda, M., Nikolich, G., King, J., & Bardin, A. R. (2014). Accounting for surface roughness on measurements conducted with PI-SWRL: Evaluation of a subjective visual approach and a photogrammetric technique. *Aeolian Research*, 13, 35–50. <https://doi.org/10.1016/j.aeolia.2014.03.002>
- Etyemezian, V., Nikolich, G., Ahonen, S., Pitchford, M., Sweeney, M., Gillies, J., & Kuhns, H. (2007). The Portable In-Situ Wind Erosion Laboratory (PI-SWRL): A new method to measure PM10 windblown dust properties and potential for emissions. *Atmospheric Environment*, 41(18), 3789–3796. <https://doi.org/10.1016/j.atmosenv.2007.01.018>
- Fécan, F., Marticorena, B., & Bergametti, G. (1999). Parametrization of the increase of the aeolian erosion thresholds wind friction velocity due to soil moisture for arid and semi-arid areas. *Annales de Geophysique*, 17(1), 149–157. <https://doi.org/10.1007/s00585-999-0149-7>
- Fierstein, J., & Hildreth, W. (1992). The plinian eruptions of 1912 at Novarupta, Katmai National Park, Alaska. *Bulletin of Volcanology*, 54(8), 646–684. <https://doi.org/10.1007/BF00430778>
- Fierstein, J., & Wilson, C. J. N. (2005). Assembling an ignimbrite: Compositionally defined eruptive packages in the 1912 Valley of Ten Thousand Smokes ignimbrite, Alaska. *Geological Society of America Bulletin*, 117(7), 1094. <https://doi.org/10.1130/b25621.1>

- Folch, A., Mingari, L., Osores, M. S., & Collini, E. (2014). Modeling volcanic ash resuspension—Application to the 14–18 October 2011 outbreak episode in central Patagonia, Argentina. *Natural Hazards and Earth System Sciences*, *14*, 119–133. <https://doi.org/10.5194/nhess-14-119-2014>
- Fowler, W. B., & Lopushinsky, W. (1986). Wind-blown volcanic ash in forest and agricultural locations as related to meteorological conditions. *Atmospheric Environment*, *20*(3), 421–425. [https://doi.org/10.1016/0004-6981\(86\)90081-8](https://doi.org/10.1016/0004-6981(86)90081-8)
- Gardner, C. A., Cashman, K. V., & Neal, C. A. (1998). Tephra-fall deposits from the 1992 eruption of Crater Peak, Alaska: Implications of clast textures for eruptive processes. *Bulletin of Volcanology*, *59*(8), 537–555. <https://doi.org/10.1007/s004450050208>
- Gillette, D., Ono, D., & Richmond, K. (2004). A combined modeling and measurement technique for estimating windblown dust emissions at Owens (dry) Lake, California. *Journal of Geophysical Research*, *109*, F01003. <https://doi.org/10.1029/2003jf000025>
- Gillette, D. A. (1979). Environmental factors affecting dust emission by wind erosion. In C. Morales (Ed.), *Saharan Dust*, (pp. 71–91). Chichester: Wiley.
- Gillette, D. A., Adams, J., Endo, E., & Smith, D. (1980). Threshold velocities for input of soil particles into the air by desert soils. *Journal of Geophysical Research*, *85*(C10), 5621–5630. <https://doi.org/10.1029/JC085iC10p05621>
- Gillette, D. A., Adams, J., Muhs, D., & Kihl, R. (1982). Threshold friction velocities and rupture moduli for crusted desert soils for the input of soil particles into the air. *Journal of Geophysical Research*, *87*(C11), 9003–9015. <https://doi.org/10.1029/JC087iC11p09003>
- Gillette, D. A., & Stockton, P. H. (1986). Mass momentum and kinetic energy fluxes of saltating particles. In W. G. Nickling (Ed.), *Aeolian Geomorphology*, (pp. 35–56). Boston, London, Sydney: Allen and Unwin.
- Gillies, J. A. (2013). Fundamentals of aeolian sediment transport/dust emissions and transport – near surface. In J. Shroder, & N. Lancaster (Eds.), *Treatise on Geomorphology*, (Vol. 11, pp. 43–63). San Diego, CA: Academic Press. <https://doi.org/10.1016/B978-0-12-374739-6.00297-9>
- Gillies, J. A., Etyemezian, V., Nikolich, G., Nickling, W. G., & Kok, J. F. (2018). Changes in the saltation flux following a step-change in macro-roughness. *Earth Surface Processes and Landforms*, *43*(9), 1871–1884. <https://doi.org/10.1002/esp.4362>
- Gillies, J. A., & Lancaster, N. (2013). Large roughness element effects on sand transport, Oceano Dunes, California. *Earth Surface Processes and Landforms*, *38*, 785–792. <https://doi.org/10.1002/esp.3317>
- Gillies, J. A., Nickling, W. G., & King, J. (2007). Shear stress partitioning in large patches of roughness in the atmospheric inertial sublayer. *Boundary-Layer Meteorology*, *122*, 367–396. <https://doi.org/10.1007/s10546-006-9101-5>
- Goldsteh, I., Ahmadi, G., & Ferro, A. (2012). A model for removal of compact, rough, irregularly shaped particles from surfaces in turbulent flows. *The Journal of Adhesion*, *88*, 829–840. <https://doi.org/10.1080/00218464.2012.694278>
- Gomes, L., Bergametti, G., Coude-Gaussen, G., & Rognon, P. (1990). Submicron desert dusts: a sandblasting process. *Journal of Geophysical Research*, *95*(D9), 13,927–13,935. <https://doi.org/10.1029/JD095iD09p13927>
- Gomes, L., Rajot, J. L., Alfaro, S. C., & Gaudichet, A. (2003). Validation of a dust production model from measurements performed in semi-arid agricultural areas of Spain and Niger. *Catena*, *52*(3–4), 257–271. [https://doi.org/10.1016/S0341-8162\(03\)00017-1](https://doi.org/10.1016/S0341-8162(03)00017-1)
- Gordian, M. E., Ozkaynak, H., Xue, J., Moris, S. S., & Spengler, J. D. (1996). Particulate air pollution and respiratory disease in Anchorage, Alaska. *Environmental Health Perspectives*, *104*(3), 290–297. <https://doi.org/10.1289/ehp.96104290>
- Gordon, M., & McKenna Neuman, C. (2009). A comparison of collisions of saltating grains with loose and consolidated silt surfaces. *Journal of Geophysical Research*, *114*, F04015. <https://doi.org/10.1029/2009JF001330>
- Guffanti, M., Mayberry, G. C., Casadevall, T. J., & Wunderman, R. (2009). Volcanic hazards to airports. *Natural Hazards*, *51*(2), 287–302. <https://doi.org/10.1007/s11069-008-9254-2>
- Hadley, D., Hufford, G., & Simpson, J. (2004). Resuspension of relic volcanic ash and dust from Katmai: Still an aviation hazard. *Weather and Forecasting*, *19*(5), 829–840. [https://doi.org/10.1175/1520-0434\(2004\)019<0829:RORVAA>2.0.CO;2](https://doi.org/10.1175/1520-0434(2004)019<0829:RORVAA>2.0.CO;2)
- Hildreth, W., & Fierstein, J. (2012). Eruptive history of Mount Katmai, Alaska. *Geosphere*, *8*(6), 1527–1567. <https://doi.org/10.1130/GES00817.1>
- Hobbs, P. E., Hegg, D. A., & Radke, L. F. (1983). Resuspension of volcanic ash from Mount St. Helens. *Journal of Geophysical Research*, *88*(C6), 3919–3921. <https://doi.org/10.1029/JC088iC06p03919>
- Holcombe, T. L., Ley, T., & Gillette, D. A. (1997). Effects of prior precipitation and source area characteristics on threshold wind velocities for blowing dust episodes, Sonoran Desert 1948–78. *Journal of Applied Meteorology*, *36*(9), 1160–1175. [https://doi.org/10.1175/1520-0450\(1997\)036<1160:EOPPAS>2.0.CO;2](https://doi.org/10.1175/1520-0450(1997)036<1160:EOPPAS>2.0.CO;2)
- Houser, C. A., & Nickling, W. G. (2001a). The emission and vertical flux of particulate matter <10 micrometers from a disturbed clay-crust surface. *Sedimentology*, *48*(2), 255–267. <https://doi.org/10.1046/j.1365-3091.2001.00359.x>
- Houser, C. A., & Nickling, W. G. (2001b). The factors influencing the abrasion efficiency of saltating grains on a clay-crust playa. *Earth Surface Processes and Landforms*, *26*(5), 491–505. <https://doi.org/10.1002/esp.193>
- Ishizuka, M., Mikami, M., Leys, J. F., Shao, Y., Yamada, Y., & Heidenreich, S. (2014). Power law relation between size-resolved vertical dust flux and friction velocity measured in a fallow wheat field. *Aeolian Research*, *12*, 87–99. <https://doi.org/10.1016/j.aeolia.2013.11.002>
- ISO (2009). International Organization for Standardization ISO 13320:2009: Particle size analysis—Laser diffraction methods, 51 pp, <https://www.iso.org/standard/44929.html>.
- Iversen, J. D., & White, B. R. (1982). Saltation threshold on Earth, Mars, and Venus. *Sedimentology*, *29*(1), 111–119. <https://doi.org/10.1111/j.1365-3091.1982.tb01713.x>
- Kenny, L. C., Gussman, R., & Meyer, M. (2000). Development of a sharp-cut cyclone for Ambient Aerosol Monitoring Applications. *Aerosol Science and Technology*, *32*(4), 338–358. <https://doi.org/10.1080/027868200303669>
- King, J., Nickling, W. G., & Gillies, J. A. (2005). Representation of vegetation and other non-erodible elements in aeolian sediment transport models. *Journal of Geophysical Research*, *110*, F04015. <https://doi.org/10.1029/2004JF000281>
- Kok, J. F., Parteli, E. J. R., Michaels, T. I., & Bou Karam, D. (2012). The physics of wind-blown sand and dust. *Reports on Progress in Physics*, *75*(10), 106901. <https://doi.org/10.1088/0034-4885/75/10/106901>
- Leadbetter, S. J., Hort, M. C., von Löwis, S., Weber, K., & Witham, C. S. (2012). Modeling the resuspension of ash deposited during the eruption of Eyjafjallajökull in spring 2010. *Journal of Geophysical Research*, *117*, D00U10. <https://doi.org/10.1029/2011jd016802>
- Liu, E. J., Cashman, K. V., Beckett, F. M., Witham, C. S., Leadbetter, S. J., Hort, M. C., & Guðmundsson, S. (2014). Ash mists and brown snow: Remobilization of volcanic ash from recent Icelandic eruptions. *Journal of Geophysical Research: Atmospheres*, *119*, 9463–9480. <https://doi.org/10.1002/2014JD021598>
- Lu, H., Raupach, M. R., & Richards, K. S. (2005). Modeling entrainment of sedimentary particles by wind and water: A generalized approach. *Journal of Geophysical Research*, *110*, D24114. <https://doi.org/10.1029/2005JD006418>

- MacKinnon, D. J., Clow, G. D., Tigges, R. K., Reynolds, R. L., & Chavez, P. S. (2004). Comparison of aerodynamically and model-derived roughness lengths (z_0) over diverse surfaces, central Mojave Desert, California, USA. *Geomorphology*, 63(1-2), 103–113. <https://doi.org/10.1016/j.geomorph.2004.03.009>
- Manville, V., & Wilson, C. J. N. (2004). The 26.5 ka Oruanui eruption, New Zealand: A review of the roles of volcanism and climate in the post-eruptive sedimentary response. *New Zealand Geological Geophysics*, 47(3), 525–547. <https://doi.org/10.1080/00288306.2004.9515074>
- Marticorena, B. (2014). Dust production mechanisms. In P. Knippertz, & J. B. Stuut (Eds.), *Mineral Dust*, (pp. 93–120). Dordrecht: Springer.
- Marticorena, B., & Bergametti, G. (1995). Modeling the atmospheric dust cycle: 1. Design of a soil-derived dust emission scheme. *Journal of Geophysical Research*, 100(D8), 16,415–16,430. <https://doi.org/10.1029/95JD00690>
- Martin, R. L., & Kok, J. F. (2017). Linear scaling of wind-driven sand flux with shear stress. *Science Advances*, 3, e1602569. <https://doi.org/10.1126/sciadv.1602569>
- McKenna Neuman, C. (2003). Effects of temperature and humidity upon the entrainment of sedimentary particles by wind. *Boundary-Layer Meteorology*, 108(1), 61–89. <https://doi.org/10.1023/A:1023035201953>
- McKenna Neuman, C. (2004). Effects of temperature and relative humidity upon the transport of sedimentary particles by wind. *Sedimentology*, 51(1), 1–17. <https://doi.org/10.1046/j.1365-3091.2003.00604.x>
- McKenna Neuman, C., & Nickling, W. G. (1989). A theoretical and wind tunnel investigation of the effect of capillary water on the entrainment of sediment by wind. *Canadian Journal of Soil Science*, 69(1), 79–96. <https://doi.org/10.4141/cjss89-008>
- McKenna Neuman, C., & Sanderson, S. (2008). Humidity control of particle emissions in aeolian systems. *Journal of Geophysical Research*, 113, F02S14. <https://doi.org/10.1029/2007JF000780>
- Miller, E. R. (1934). Meteorology of the dustfall of November 12–13, 1933. *Journal of Sedimentary Petrology*, 4, 78–81. <https://doi.org/10.1306/d4268ebe-2b26-11d7-8648000102c1865d>
- Mingari, L. A., Collini, E. A., Folch, A., Báez, W., Bustos, E., Osoro, M. S., et al. (2017). Numerical simulations of windblown dust over complex terrain: The Fiambalá Basin episode in June 2015. *Atmospheric Chemistry and Physics*, 17(11), 6759–6778. <https://doi.org/10.5194/acp-17-6759-2017>
- Minvielle, F., Marticorena, B., Gillette, D. A., Lawson, R. E., Thompson, R., & Bergametti, G. (2003). Relationship between the aerodynamic roughness length and the roughness density in cases of low roughness density. *Journal of Fluid Mechanical Engineering*, 3(3), 249–267. <https://doi.org/10.1023/A:1022830119554>
- Moen, W., & McLucas, B. (1981). *Mount St. Helens Ash, properties and possible uses*. State of Washington: Department of Natural Resources, Division of Geology and Earth Resources. 1981
- Munkhtsetseg, E., Shinoda, M., Gillies, J. A., Kimura, R., King, J., & Nikolich, G. (2016). Relationships between soil moisture and dust emissions in a bare sandy soil of Mongolia. *Particulology*, 28, 131–137. <https://doi.org/10.1016/j.partic.2016.03.001>
- Ngan, F., & Stein, A. (2017). A long-term WRF meteorological archive for dispersion simulations: Application to controlled tracer experiments. *Journal of Applied Meteorology and Climatology*, 56(8), 2203–2220. <https://doi.org/10.1175/JAMC-D-16-0345.1>
- Nickling, W. G. (1978). Eolian sediment transport during dust storms: Slims River Valley, Yukon Territory. *Canadian Journal of Earth Sciences*, 15(7), 1069–1084. <https://doi.org/10.1139/e78-114>
- Nickling, W. G., & Ecclestone, M. (1981). The effects of soluble salts on the threshold shear velocity of fine sand. *Sedimentology*, 28(4), 505–510. <https://doi.org/10.1111/j.1365-3091.1981.tb01698.x>
- Nickling, W. G., & Gillies, J. A. (1993). Dust emission and transport in Mali, West Africa. *Sedimentology*, 40(5), 859–868. <https://doi.org/10.1111/j.1365-3091.1993.tb01365.x>
- Nickling, W. G., McTainsh, G. H., & Leys, J. F. (1999). Dust emissions from the Channel Country of western Queensland, Australia. *Zeitschrift für Geomorphologie Supplementband*, 116, 1–17.
- Niemeyer, T. C., Gillette, D. A., Deluisi, J. J., Kim, Y. J., Niemeyer, W. F., Ley, T., et al. (1999). Optical depth, size distribution and flux of dust from Owens Lake, California. *Earth Surface Processes and Landforms*, 24(5), 463–479. [https://doi.org/10.1002/\(SICI\)1096-9837\(199905\)24:5<463::AID-ESP2>3.0.CO;2-R](https://doi.org/10.1002/(SICI)1096-9837(199905)24:5<463::AID-ESP2>3.0.CO;2-R)
- Pierre, C., Bergametti, G., Marticorena, B., Kergoat, L., Mougou, E., & Hiernaux, P. (2014). Comparing drag partition schemes over a herbaceous Sahelian rangeland. *Journal of Geophysical Research: Solid Earth*, 119, 2291–2313. <https://doi.org/10.1002/2014JF003177>
- Prandtl, L. (1935). The mechanics of viscous fluids. In F. Durand (Ed.), *Aerodynamic Theory*, (pp. 57–100). Berlin: Springer-Verlag. https://doi.org/10.1007/978-3-642-91486-7_2
- Raupach, M. R., Gillette, D. A., & Leys, J. F. (1993). The effect of roughness elements on wind erosion threshold. *Journal of Geophysical Research*, 98(D2), 3023–3029. <https://doi.org/10.1029/92JD01922>
- Ravi, S., & D'Odorico, P. (2005). A field-scale analysis of the dependence of wind erosion threshold velocity on air humidity. *Geophysical Research Letters*, 32, L21404. <https://doi.org/10.1029/2005gl023675>
- Ravi, S., D'Odorico, P., Over, T. M., & Zobeck, T. M. (2004). On the effect of air humidity on soil susceptibility to wind erosion: The case of air-dry soils. *Geophysical Research Letters*, 31, L09501. <https://doi.org/10.1029/2004GL019485>
- Ravi, S., Zobeck, T. M., Over, T. M., Okin, G. S., & D'Odorico, P. (2006). On the effect of moisture bonding forces in air-dry soils on threshold friction velocity of wind erosion. *Sedimentology*, 53, 597–609. <https://doi.org/10.1111/j.1365-3091.2006.00775.x>
- Reckziegel, F., Bustos, E., Mingari, L., Baez, W., Villarosa, G., Folch, A., et al. (2016). Forecasting volcanic ash dispersal and coeval resuspension during the April–May 2015 Calbuco eruption. *Journal of Volcanology and Geothermal Research*, 321, 44–57. <https://doi.org/10.1016/j.jvolgeores.2016.04.033>
- Sarna-Wojcicki, A. M., Shipley, S., Waitt, R., Dzurisin, D., & Wood, S. H. (1981). In P. W. Lipman, & R. L. Christiansen (Eds.), *Areal distribution, thickness, mass, volume, and grain size of air-fall ash from the six major eruptions of 1980, in the 1980 Eruptions of Mount St. Helens, Washington, Professional Paper*, (Vol. 1250, pp. 577–601). Washington, DC: U.S. Geological Survey.
- Schwaiger, H.F., & Wallace, K. (2015). Modelling the resuspension of volcanic ash from the Valley of Ten Thousand Smokes. *AGU Fall Meeting Abstracts*, Dec. 2015.
- Scollo, S., Del Carlo, P., & Coltelli, M. (2007). Tephra fallout of 2001 Etna flank eruption: Analysis of the deposit and plume dispersion. *Journal of Volcanology and Geothermal Research*, 160(1-2), 147–164. <https://doi.org/10.1016/j.jvolgeores.2006.09.007>
- Sehmel, G. A. (1982). Ambient airborne solids concentrations including volcanic ash at Hanford, Washington sampling sites subsequent to the Mount St. Helens eruption. *Journal of Geophysical Research*, 87(C13), 11,087–11,094. <https://doi.org/10.1029/JC087iC13p11087>
- Shao, Y. (2000). *Physics and modelling of wind erosion*, (p. 393). Dordrecht: Kluwer Academic Publishers.
- Shao, Y., & Lu, H. (2000). A simple expression for wind erosion threshold friction velocity. *Journal of Geophysical Research*, 105(D17), 22,437. <https://doi.org/10.1029/2000jd900304>
- Shao, Y., Raupach, M. R., & Findlater, P. A. (1993). The effect of saltation bombardment on the entrainment of dust by wind. *Journal of Geophysical Research*, 98(D7), 12,719–12,726. <https://doi.org/10.1029/93JD00396>

- Shao, Y., & Yang, Y. (2008). A theory for drag partition over rough surfaces. *Journal of Geophysical Research*, *113*, F02S05. <https://doi.org/10.1029/2007JF000791>
- Smith, A., Lott, N., & Vose, R. (2011). The integrated surface database: Recent developments and partnerships. *Bulletin of the American Meteorological Society*, *92*(6), 704–708. <https://doi.org/10.1175/2011BAMS3015.1>
- Sow, M., Alfaro, S. C., Rajot, J. L., & Marticorena, B. (2009). Size resolved dust emission fluxes measured in Niger during 3 dust storms of the AMMA experiment. *Atmospheric Chemistry and Physics*, *9*(12), 3881–3891. <https://doi.org/10.5194/acp-9-3881-2009>
- Sweeney, M., Etyemezian, V., Macpherson, T., Nickling, W. G., Gillies, J., Nikolich, G., & McDonald, E. (2008). Comparison of PI-SWERL with dust emission measurements from a straight-line field wind tunnel. *Journal of Geophysical Research*, *113*, F01012. <https://doi.org/10.1029/2007JF000830>
- Sweeney, M., Lu, H. Y., Cui, M. C., Mason, J. A., Feng, H., & Xu, Z. W. (2016). Sand dunes as potential sources of dust in northern China. *Science China Earth Sciences*, *59*(4), 760–769. <https://doi.org/10.1007/s11430-015-5246-8>
- Sweeney, M., McDonald, E. V., & Etyemezian, V. (2011). Quantifying dust emissions from desert landforms. *Geomorphology*, *135*(1-2), 21–34. <https://doi.org/10.1016/j.geomorph.2011.07.022>
- Sweeney, M. R., & Mason, J. A. (2013). Mechanisms of dust emission from Pleistocene loess deposits, Nebraska, USA. *Journal of Geophysical Research: Solid Earth*, *118*, 1460–1471. <https://doi.org/10.1002/jgrf.20101>
- Thorsteinsson, T., Gísladóttir, G., Bullard, J., & McTainsh, G. (2011). Dust storm contributions to airborne particulate matter in Reykjavik, Iceland. *Atmospheric Environment*, *45*(32), 5924–5933. <https://doi.org/10.1016/j.atmosenv.2011.05.023>
- Thorsteinsson, T., Jóhannsson, T., Stohl, A., & Kristiansen, N. I. (2012). High levels of particulate matter in Iceland due to direct ash emissions by the Eyjafjallajökull eruption and resuspension of deposited ash. *Journal of Geophysical Research*, *117*, B00C05. <https://doi.org/10.1029/2011jb008756>
- US DOE (2012). EM-QA-001 Rev 1: EM Quality Assurance Program (QAP), Office Of Environmental Management, US Department of Energy, June 11, 2012.
- Wallace, K. L., & Schwaiger, H. F. (2019). Volcanic ash resuspension from the Katmai Region. *Alaska Park Science*, *18*(1), 47–53.
- Webley, P. W. (2013). Re-suspended ash seen from Katmai Volcano region, first detected 07:24 UTC May 18 2013, in <http://www.volcanodetect.blogspot.com/2013/05/re-suspended-ashseen-from-katmai>.
- Willets, B. B., Rice, M. A., & Swaine, S. E. (1982). Shape effects in aeolian grain transport. *Sedimentology*, *29*(3), 409–417. <https://doi.org/10.1111/j.1365-3091.1982.tb01803.x>
- Williams, G. (1964). Some aspects of the aeolian saltation load. *Sedimentology*, *3*(4), 257–287. <https://doi.org/10.1111/j.1365-3091.1964.tb00642.x>
- Wilson, T. M., Cole, J. W., Stewart, C., Cronin, S. J., & Johnston, D. M. (2011). Ash storms: Impacts of wind-remobilised volcanic ash on rural communities and agriculture following the 1991 Hudson eruption, southern Patagonia, Chile. *Bulletin of Volcanology*, *73*(3), 223–239. <https://doi.org/10.1007/s00445-010-0396-1>
- Wolfe, S. A., & Nickling, W. G. (1993). The protective role of sparse vegetation in wind erosion. *Progress in Physical Geography*, *17*(1), 50–68. <https://doi.org/10.1177/030913339301700104>